SPACE SCIENCE AND GEOSPATIAL INSTITUTE

ENTOTO OBSERVATORY AND RESEARCH CENTER

ASTRONOMY AND ASTROPHYSICS DEPARTMENT
SCHOOL OF GRADUATE STUDIES

X-ray and radio properties of far-infrared green valley active galaxies

By
Samuel Bogale Worku

November, 2022

Addis Ababa, Ethiopia

DECLARATION

I hereby declare that this MSc thesis entitled "**X-ray and radio properties of far-infrared green valley active galaxies**" is original and has never been submitted to any other institutions, to the best of my knowledge.

Samuel Bogale Worku _____
Full Name Signature

This thesis has been submitted for examination with my approval as an advisor.

Mirjana Pović _____
Name Signature

Submitted to: Entoto Observatory, Space Science and Geospatial Institute Astronomy and Astrophysics Department

_____
Date of submission

Abstract

We analysed a sample of 1472 X-ray detected AGN in the COSMOS field. Recently it has been seen that, within the same stellar mass range, green valley (GV) selected far-infrared (FIR) AGN show enhanced star formation rates (SFR) in comparison to non-AGN sources, opposite of what has been suggested in previous optical and X-ray studies. In this work, we went a step further and performed a multiwavelength study in optical, X-rays, and radio of the GV AGN. In addition, we extended our study to the blue cloud (BC) and red sequence (RS) AGN selected through the commonly used U-B rest-frame colour criteria. We analysed different properties in X-rays using several bands, such as the X-ray-to-optical flux ratio, hardness ratios, X-ray luminosities, the location of sources on the X/O-hardness ratio plane, on the X-ray luminosity-redshift plane, and on the X-ray luminosity-stellar mass plane. In radio, we analysed the distribution of BC, GV, and RS AGN regarding the radio luminosities at 1.4 GHz and 3 GHz, X-ray to radio luminosity ratio, accretion rates, jet luminosity, and also radio classification. Finally, we analysed the distribution of SFR and black hole mass of BC, GV, and RS AGN, as well as their location in terms of the main-sequence of star formation. BC, GV, and RS active galaxies show in general very similar properties in X-rays and radio, covering a rather narrow than broad range of all analysed parameters. We confirmed the results and found that in addition to GV AGN, BC and RS FIR AGN also show enhanced SFRs, once again in contradiction to previous studies carried out in optical, confirming more complex scenarios of the role of AGN in star formation quenching when using multiwavelength data and the need for further studies.

Acknowledgment

First and foremost, I would like to thank my heavenly father and my savior for everything he has done in my life and giving me gudiness when I needed the most. Secondly, I want to thank my parents for their support and for not giving up on my dream. Finally, I would like to thank my advisor Dr Mirjana Pović for her wise counsel, unwavering support, and tolerance. Her vast knowledge and experience have inspired me in my academic research.

Contents

List of Abbreviations

- ACS - Advanced Camera for Surveys
- AGN - Active Galactic Nuclei
- ALH survey - ALHAMBRA survey
- BC - Blue Cloud
- BL Lac - BL Lacertae
- BLR - Broad Line Regions
- BPT - Baldwin-Phillips-Terlevich diagram
- BPZ - Bayesian Photometric Redshifts
- CMD - Colour-Magnitude Diagram
- COSMOS - Cosmic Evolution Survey
- CR - Count Rates
- DEC - Declination
- ET - Early-type
- FIR - Far-Infrared
- FR - Fanaroff-Riley
- FSRQ - Flat-Spectrum Radio Quasars
- FUV - Far-Ultraviolet
- GALEX - Galaxy Evolution Explorer
- GV - Green Valley
- HLAGN- Moderate-to-High Radiative Luminosity AGN

- HST - Hubble Space Telescope
- IMF - Initial Mass Function
- ISM - Interstellar Medium
- LINERs - Low-Ionization Nuclear Emission-Line Regions
- LT - Late-type
- MBH - Black Hole Mass
- MS - Main Sequence (of star formation)
- MIR - Mid Infrared
- MLAGN AGN- Low-to-Moderate Radiative Luminosity AGN
- NLR Narrow Line Regions
- NRAO NVSS - National Radio Astronomy Observatory VLA Sky Survey
- OVV - Optically Violent Variable Quasar
- PACS - Photodetector Array Camera and Spectrometer
- PCC - Pearson Correlation Coefficient
- QMLAGN - Quiescent Low-to-Moderate Radiative Luminosity AGN
- RA - Right Ascension
- RLQ - Radio-Loud Quasars
- RQQ - Radio-Quiet Quasars
- RS - Red Sequence
- SDSS - Sloan Digital Sky Survey
- SED - Spectral Energy Distribution
- SF - Star Formation
- SFG - Star-forming galaxies
- SFH - Star Formation History
- SFR - Star Formation Rate
- SMBH - Supermassive Black Hole

- sSFR - Specific Star Formation Rate
- SSRQ - Steep-Spectrum Radio Quasars
- TOPCAT - Tool for OPerations on Catalogues And Tables
- UV - Ultraviolet
- VLA - Very Large Array

List of Figures

List of Tables

Chapter 1

Introduction

1.1 General overview

The bi-modal distribution of galaxies observed in colour-mass, colour-magnitude, colour-colour, or colour-star formation rate diagrams has been studied to understand the properties of galaxies and their evolution. In these diagrams, galaxies are mainly concentrated in two regions, the blue cloud (BC) and red sequence (RS). The BC is predominantly populated by late-type (LT) galaxies (like spirals) with active star formation (SF), while the RS is mainly populated by early-type (ET) galaxies (elliptical and lenticular) (e.g., Kauffmann et al. (2003); Baldry et al. (2004); Salim et al. (2007); Brammer et al. (2009); Pović et al. (2013); Schawinski et al. (2014); Lee et al. (2015); Ge et al. (2018); Phillips et al. (2019)). The region between the BC and RS, less populated with galaxies, is called green valley (GV). Previous works suggested that GV is a transition region, important to study for understanding the process of star formation quenching and how galaxies transform from LT to ET (e.g., Schawinski et al. (2014)).

Previous studies suggested that most of the X-ray and optically detected active galactic nuclei (AGN) are located in GV, between the BC and RS (e.g., Nandra et al. (2007); Pović et al. (2012); Zewdie et al. (2020)). They can be hosted by both ET and LT galaxies, and different works suggested that AGN negative feedback might be responsible for quenching SF in galaxies. Therefore, the AGN host galaxies selected in the optical and X-rays tend to have star formation rates (SFRs) lower than typical main-sequence star-forming galaxies (e.g., Ellison et al. (2016); Smith et al. (2016); Leslie et al. (2016); Sánchez et al. (2018); Lacerda et al. (2020)). However, recently, observing the location of X-ray detected AGN and non-AGN galaxies with FIR emission on the main sequence of SF in the COSMOS field, different results have been found in comparison to optical and X-ray studies (Mahoro et al. (2017)). Rather than having lower SFRs, X-ray detected AGN with FIR emission showed higher SFRs at fixed stellar mass ranges. These results suggested that selected sample of FIR AGN does

not show signs of SF quenching but rather its enhancement, independently of morphology (Mahoro et al. 2019). The authors also didn't find older stellar populations in the FIR AGN sample in comparison to non-AGN (Mahoro et al. (2022)), as previously suggested. The authors suggested the possibility of having an effect of positive AGN feedback in the selected sample.

Although lots of improvement has been made over the last years regarding the properties of GV galaxies and SF quenching mechanisms in galaxies, there are still many open questions. For example, what is the role of AGN in galaxy evolution and SF quenching especially when using multi-wavelength data and analysis, what is the fraction of GV galaxies, what is the fraction of AGN and non-AGN galaxies in the GV, why FIR AGN show higher SFRs, what is the role of AGN positive and negative feedback in galaxies evolution, etc. In this work, we plan to go a step further to understand better the type of active galaxies studied in Mahoro et al. (2017, 2019, 2022) by analyzing the whole sample of X-ray detected AGN in the COSMOS survey. This will help us to understand better the results obtained by authors, in terms of both properties of active and non-active galaxies in GV and the role that AGN may have in SF quenching and galaxy evolution. We will use X-ray and radio data to distinguish between different AGN types, but also optical spectroscopic data when available. We will compare the properties of those AGN selected in the GV by Mahoro et al. (2017), with AGN located in the BC and RS.

This thesis is structured as follows: in chapter 1, the general overview, objectives of the study, and the significance of the work. In chapter 2, we provide the literature review about the general properties of galaxies, the properties of galaxies in GV, and the role of AGN in star formation quenching and galaxy evolution. Data used are explained in chapter 3, whereas chapter 4 the analysis carried out in optical, X-rays and radio and obtained results. Finally, chapters 5 give the discussion, and main conclusions, respectively.

1.2 Objectives of the study

1.2.1 General objective

The general objective of this work is to better understand the FIR emitting AGN in the COSMOS field with higher SFR than the non AGN galaxies, and give an information towards understanding a possible role of AGN in SF quenching in galaxies and galaxy evolution.

1.2.2 Specific objectives

On the way of addressing the above general objective, our specific objectives are:

- To carry out the X-ray study of a selected green valley detected AGN with FIR emission in the COSMOS field.
- To carry out the radio study of the same sample of active galaxies.
- To compare X-ray and radio properties with other properties such as SFR, stellar mass, and AGN spectroscopic type (when optical spectroscopic data are available).
- To compare selected GV AGN with BC and RS active galaxies in terms of their multi-wavelength properties.

1.3 Significance of the work

Results obtained in Mahoro et al. (2017, 2019, 2022) with X-ray detected AGN with FIR emission showing enhanced SFRs instead of quenched SF activity are, in our knowledge, some of the very first and few (if not only) results of such kind. This shows that more multi-wavelength studies is needed to understand fully the SF quenching in galaxies and galaxy evolution from LT to ET galaxies. Through the multi-wavelength study suggested to be carried out in this work is to understand better the type of AGN activity and try to get a more clear picture of the possible role of AGN in SF properties of GV galaxies.

Chapter 2

Literature Review

2.1 General properties of galaxies

This section summarises some of the main properties of galaxies and some of the relations between them studied in many of previous works (e.g., Salim et al. (2007); Pović et al. (2012); Pan et al. (2013); Pović et al. (2013); Salim (2014); Schawinski et al. (2014); Lee et al. (2015); Smethurst et al. (2015); Trayford et al. (2016); Coenda, Martínez and Muriel (2018); Ge et al. (2018); Phillips et al. (2019)).

2.1.1 Summary of basic properties of galaxies

1. **Brightness parameters**

   Brightness is a fundamental parameter used to describe a galaxy. It is crucial in many aspects of extra-galactic astronomy and cosmology, from identifying the entire family of galaxy populations to modelling their various distributions and motions in the universe. These aspects are generally related to galaxy formation and evolution as well as the nature of large-scale structures in the Universe (e.g., Z. Shao et al. (2003), and references therein). The brightness of a celestial source can be expressed in terms of apparent and absolute magnitude, flux (or flux density) and luminosity.

   Apparent magnitude is the brightness measured by an observer at a specific distance from the object (Hughes et al. (2006), and reference therein). We can calculate the apparent magnitude using the following formula:

   $$m_2 - m_1 = -2.5 \log(B2/B1), \tag{2.1}$$

   where $B2/B1$ is the ratio of brightness (flux) and $m_2 - m_1$ the difference in magnitude of two celestial sources.

   Absolute magnitude is a measure of the star's or galaxy's intrinsic brightness which refers to how bright the star or galaxy would be if viewed from the distance of 10 parsecs

(Hughes et al. (2006), and reference therein). This can be expressed as:

$$M = m - 2.5 \log \left(\frac{d}{10} \right)^2, \tag{2.2}$$

where d is distance in parsec, M is absolute magnitude and m is apparent magnitude.

Flux is the total amount of energy that crosses a unit area per unit time. Flux is measured in joules per square meter per second (joules/m^2/s), or watts per square meter (watts/m^2). It can also be measured in erg/sec/cm^2, which is the unit commonly used in astronomy (Edge et al. (1992)). In the AB photometric system of magnitudes, commonly used in modern photometric surveys, flux can be measured through the flux density and apparent magnitude as:

$$m_{AB} = -2.5 \log_{10} f_\nu - 48.60. \tag{2.3}$$

The apparent magnitude in this equation, denoted by the symbol m$_{AB}$, and the flux density, denoted by the symbol fν, are both expressed in ergs^{-1} cm^{-2} Hz^{-1} in SI unit.

Luminosity is an intrinsic measure of the celestial source brightness which can be measured through the flux using the following equation:

$$F = \frac{L}{4\pi d_l^2}, \tag{2.4}$$

where F is a flux measured at distance d$_l$, L is luminosity of the source, d$_l$ is distance to the source. There is a wide range in the overall luminosity of the galaxies going, from dwarf galaxies with the luminosity of several hundreds of thousands of solar luminosity (L$_\odot$), up to the luminosity of the brightest active galaxies of up to 10^{15}-10^{16} L$_\odot$. The typical luminosity of normal large spiral galaxies are a few hundred billion of L$_\odot$ (e.g., Z. Shao et al. (2003), and references therein).

2. The colours of galaxies

Colour can be defined as a difference between the two magnitudes obtained in two different photometric bands. The colour of galaxies usually depends on the type of stars (or stellar populations) they contain. For example, if there is a large amount of old red stars, the galaxy appears to have a reddish colour. On the other side, if there is a large amount of young, massive, blue stars, then it becomes bluish (e.g., Schawinski et al. (2014), and references therein). In addition to the stellar populations, the presence of AGN, star formation, extinction, or galaxy inclination, can also affect galaxy colour. Therefore, colour is one of the key parameters of galaxies, being related to many other

galaxy properties, such as its mass or SFR. For example, red galaxies in the local Universe often show higher stellar masses than blue galaxies whereas, blue galaxies tend to have higher SFRs. The colour of galaxies can also give information about the present-day stars and hints about the formation and evolution of galaxies (e.g., Pović et al. (2012); Salim (2014); Schawinski et al. (2014); Xu et al. (2018); Calzetti et al. (2022); Stephen et al. (2022)). Using the colour galaxy can be classified into RS, BC, and GV, as mentioned above (e.g., Salim (2014); Schawinski et al. (2014), and references therein).

3. Morphology

Morphology is one of the fundamental parameters for understanding the whole picture of galaxy formation and evolution with cosmic time (e.g., Conselice (2014)). It is relevant not only for providing knowledge about galaxy structure but also providing information how other parameters, such as environment, the rate of interactions and mergers, nuclear activity in galaxies, the interstellar medium, etc., affect morphology and vice-versa. Morphology can be classified into:

Elliptical galaxies are smooth and featureless, without spiral arms or dust lanes. They generally have lower amounts of the interstellar medium (ISM), with little or no active star formation. Elliptical galaxies are known to be the most massive stellar systems in the local Universe, which appear to be defined in a homogeneous class with old, red stellar populations (e.g., Lucia (2006); Rogers et al. (2009); Binney et al. (2011); Eappen et al. (2022), and references therein). The stars in these galaxies are old, typically $\sim$ 10-13 Gyr. The isophotes are elliptical or spherical, generally to within a few percent accuracy. Nevertheless, most show significant variation in ellipticity and position angle with radius.

Ellipticity is defined by:

$$\varepsilon = 1 - b/a, \tag{2.5}$$

where a and b are the semi-major and semi-minor axes of the ellipse, respectively. Elliptical galaxies are classified according to apparent flattening.

Spiral galaxies are twisted collections of stars and ISM, containing galactic bulges, discs, and spiral arms. They rotate around the centre. Spiral arms are areas of high-density matter and places where star formation occurs. They can harbour many bright and young stars, such as hot OB stars, and contain high amounts of gas and dust lanes. They are divided into two subclasses: normal spirals (Ss) and barred spirals (SBs) that have a nuclear stellar bar (e.g., Schneider (2006), Mastropietro et al. (2021); Wenderoth et al. (2022), and references therein). Spiral arms, traced by young luminous stars, and large amounts of ISM, highlight regions of active star formation triggered by density waves propagating in the disc. As the sequence progresses from ET to LT spirals (from

Sa through Sb, to Sc and Sd), the spiral arms increase in prominence and become more open and more irregular in shape (e.g., Greener et al. (2022); Porter et al. (2022); Frosst et al. (2022)).

Lenticular (S0) galaxies galaxies have intermediate properties between elliptical and spiral galaxies (e.g., Johnston et al. (2012); Katkov et al. (2015); Saha and Cortesi (2018); Paci et al. (2021)). They normally show signs of a rotating disc, but the disc lacks spiral arms and active star formation. S0 galaxies are more flattened than elliptical galaxies and have a noticeable disc. However, they normally lack evidence of gas, spiral arms, star formation or young stellar populations. Many S0 galaxies have visible dust. The subclasses S01, S02, S03 designate increasing amounts of dust (e.g., Bergh (2009), and references therein).

Irregular galaxies do not have any particular shape, nor standard structure (e.g., Conselice (2006)). There are two classes of irregular galaxies according to Hubble classification:

(a) Irr-I are normal low-luminosity star-forming galaxies, that still have some signs of structure.

(b) Irr-II are peculiar systems, such as M82, without any structure.

Galaxies are often divided into two broader types, ET and LT galaxies, as defined above. Normally, ET galaxies consider ellipticals and lenticulars, while LT galaxies refer to spirals and irregular galaxies.

Peculiar galaxies form 5% to 10% of known galaxies in the local Universe. These galaxies show particular structures not commonly seen in a normal spiral or elliptical galaxies, such as rings of star formation, filaments and tails, dust lanes, jets, etc. (e.g., Kaviraj (2010); Freitas-Lemes et al. (2017); Gillman et al. (2020); Mastropietro et al. (2021); Wenderoth et al. (2022)). Very often, peculiar galaxies are related to interactions and mergers. When two galaxies are relatively close, their gravitational force can cause them to adopt radically irregular shapes. Since the majority of peculiar galaxies attribute their formation to such gravitational forces, the terms "interacting galaxy" and "peculiar galaxy" is often used in the same context (e.g., Schneider (2006); Mastropietro et al. (2021); Wenderoth et al. (2022), and references therein).

4. Redshift

Redshift (z) is a displacement of the spectrum that an astronomical object moves toward longer wavelengths. In cosmology, there are many ways to specify the distance between two points, because of the expansion of the universe. This is calculated with an

equation 2.6, where $\lambda_{observed}$ is the observed wavelength of a spectral line, and $\lambda_{emission}$ is the wavelength that line would have if its source was not in motion (e.g., Hogg (1999)):

$$z = \frac{\lambda_{observed} - \lambda_{emission}}{\lambda_{emission}}, \tag{2.6}$$

Redshifts are normally obtained using spectroscopic data and prominent emission and absorption lines, using photometric data and spectral energy distribution (SED) fitting, and/or through different machine learning techniques (e.g., Molino et al. (2014); Ruiz et al. (2018); Brescia et al. (2019); Tarrío and Zarattini (2020); Henghes et al. (2022); Dey et al. (2022)).

5. **Stellar mass**

   It is defined as the physical parameter of a galaxy formation and evolution studied as it traces the galaxy formation process. It is also one of the fundamental parameters that play a major role in determining different galaxy parameters such as SFR and specific SFR (sSFR) (e.g., Contini et al. (2019)).

6. **Star formation rate**

   The star formation rate (SFR) of galaxies is defined as the total mass of stars formed per year, often given as solar masses per year (e.g., Fuchs (2014)). SFR of a galaxy is one of important parameters used in developing our understanding of formation and evolution (e.g., Hopkins (2003); Kauffmann et al. (2003); Brinchmann et al. (2004); Madau and Dickinson (2014)). It can be measured through different techniques, in optical using the intensity of emission lines such as Hα or [OII], but also the luminosity measured in far-infrared (FIR) and ultraviolet (UV) (see the references in Mahoro et al. (2017)). Star formation in galaxies occurs in the main sequence of star formation (see section 2.1.3). When star formation is quenched, galaxies depart from the main sequence and change their colour as a result of the quenching process (e.g., Pović et al. (2012); Whitaker et al. (2012); Schawinski et al. (2014); Leslie et al. (2016); Mahoro et al. (2017), and references therein).

2.1.2 AGN

Active galaxies are known to be a special class of galaxies having a very strong energy source or AGN in their centre (e.g., Schneider et al. (2006); Ho (2008); Heckman and Best (2014); Netzer (2015); Kewley (2019)). They are known to emit up to thousands of times more energy than a normal galaxy. Most of this energy is released not in visible

light but other wavelengths, from radio waves to gamma rays (e.g., Risaliti and Elvis (2004)).

AGN are energetic astrophysical sources powered by accretion onto SMBH in galaxies and present unique observational signatures that cover the full electromagnetic spectrum. AGN are some of the most interesting and crucial sources in the universe. Their studies are connected to galaxy evolution, understanding of energy sources, galaxy morphology, interactions and merging, binary and multiple structure and clustering. Being some of the most luminous sources in the universe, they can be used as means for discovery of distant objects. On the other hand, their evolution as a function of cosmic time also puts constraints on cosmological models of the Universe (e.g., Ho (2008), Netzer (2015), Padovani et al. (2017), Lusso et al. (2019); Risaliti and Lusso (2019); Zhang et al. (2021)).

Some of the properties of active galaxies not observed in non-active ones are the following (e.g., Padovani et al. (2017)):

- Active galaxies can be up to 10,000 times or even more brighter than the non-active galaxies.
- In active galaxies the luminosity can change in factor by 2 in a short period of time. For example, they can change in few days, and sometimes can even be variable in terms of hours and minutes.
- Active galaxies can have relativistic jets and lobes, whereas non-active ones don‘t have them.
- Active galaxies have much stronger and broader emission lines than non-active galaxies, showing often more complex (asymmetric) line profiles.

Standard Model of AGN

The Standard Model of AGN is shown in figure 2.1 and includes the following components:

1. **Supermassive black hole (SMBH)** is the largest blackhole with range of masses between 10^6 up to 10^{10} $M_\odot$ located in the nucleus of every galaxy and generally surrounded by accretion disc (e.g., Woods et al. (2019), and references therein). SMBHs are common in galaxy centres and show fundamental correlations with their hosts (e.g., with galaxy bulge mass and luminosity, light concentration, velocity dispersion, etc.), indicating a strong connection between SMBH and galaxy evolution (e.g., Pović et al. (2009a,b); Beifiori et al. (2012); Davis et al. (2019); Gaspari et al. (2019); Shankar et al. (2019); Caglar et al. (2020); Bennert et al. (2021); Luo et al. (2021); Kovacević-Dojcinović et al. (2022)).

2. **Accretion disc** is a rotating disc around the SMBH that transports matter to the centre. The principle of accretion stated that gas falling onto a compact object loses its potential energy, which is first converted into kinetic energy. If the infall is not prevented, then the gas will fall into the SMBH without being able to radiate its energy (e.g., Schneider et al. (2006)). Accretion disc is surrounded by hot corona that usually emits in X-rays (e.g., Agarwal et al. (2019)). Emission from the accretion disc in UV and optical can be often absorbed by the obscuring torus (e.g., Ramos-Almeida and Ricc (2017); Ross et al. (2018), and references therein).

3. **Obscuring torus** is a compact, dusty torus, which is an essential fundamental element of AGN, and optically dense region of the wind approaching from the accretion disc with the size of parsecs (e.g., Ramos-Almeida and Ricci (2017), and references therein). It produces infrared emission and is responsible for blocking our view to the AGN. Different models have been proposed for obscuring torus, from homogeneous to clumpy. The presence of an obscuring dust torus around the main engine was first implied indirectly by the spectropolarimetric detection of broad permitted emission lines (type-1 AGN) scattered into the line of sight by free electrons located above or below the dust torus in type-2 AGN (e.g., Ramos-Almeida and Ricci (2017), and references therein).

4. **Broad and narrow line regions** (BLR and NLR, respectively) are found above the accretion disk. The heavy ionized clouds of BLR become noticeable with lines movement of 1,000-10,000 km/sec, while the NLRs are usually found far away from the BLR. The emission line of lines of NLR have lower velocities of several hundreds of km/sec (e.g., Groves (2006); Ho et al. (2008); Netzer et al. (2015); Adhikari et al. (2017); Jaderson et al. (2017)).

5. **Relativistic jets** are peculiar features that connect SMBHs and spinning black holes and their attendant discs with their host galaxies and the universe beyond. Some of the works suggest that they are formed when the SMBH spins and the accretion disc is strongly magnetized, on account of gas accreting at high latitude beyond the SMBH sphere (e.g., Veilleux (2005); Boselli (2009); Blandford and Meier (2019); Davis and Tchekhovskoy (2020)), however the origin of relativistic jets is still one of the open questions in astronomy.

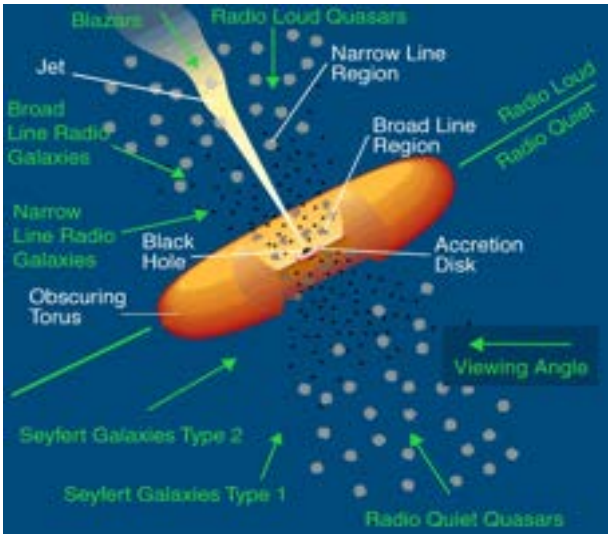

Figure 2.1: The standard and unification model of AGN. Figure is adapted from: Polletta, Urry and Padovani (1995).

Types of AGN

AGN can be classified in many different ways. Below we represent the classification of AGN taking into account the radio emission and presence/absence of radio jets, called radio-loud (RL)/radio-quiet (RQ), respectively. Under each of the two classes we described different types of AGN.

1. **Radio-loud AGN**

   - **Radio galaxies** are galaxies that are powerful radio sources. They are often associated with elliptical galaxies. The radio emission of a radio galaxy is non-thermal synchrotron radiation. The radio luminosity of radio galaxies is typically$10^{33} - 10^{38}$ W. The main challenge in explaining radio emission is determining how electrons and magnetic fields are produced and, more relevantly, where the electrons get their energy. The distinguishing feature of a strong radio galaxy is a dual structure: there are two large radio-emitting regions on opposite sides of the observed galaxies (e.g., Karttunen (2003), Sikora et al. (2020); Boizelle et al. (2021); Fukazawa et al. (2022); Garofalo et al. (2022); Slijepcevic et al. (2022), and references therein).
   - **Blazars** are a type of galaxy powered by a feeding SMBH and are among the brightest and most energetic objects. They are also RL AGN with relativistic jets seen at a

small angle to the line of sight (e.g., C. Megan Urry and Padovani (1995)). They can be divided into two groups: optically violent variable quasars (OVV), and BL Lacertae (BL Lac) type objects, which display extremely intense, broad and rapidly varying electromagnetic emission, from radio to gamma-rays (e.g., Schneider (2006); Giommi et al. (2012); Foschini (2017); Bhatta and Duda (2021)).

- **Radio loud qusars** having radio jets, are rare compared to radio-quiet quasars (e.g., Falomo et al., (2003); Barvainis et al. (2005); Zhu et al. (2021), and references therein). They are further classified as compact flat-spectrum radio quasars (FSRQ; $\alpha > 0.5$) and extended steep-spectrum radio quasars (SSRQ; $\alpha < 0.5$), with the spectral index α defined as fν α $\nu^{-\alpha}$, fν being the flux density at a given frequency. A radio-loud quasar consists of a compact central core and extended lobes. The central core's spectrum is flat, and the lobe spectra are steep. The radio-active quasar appears as an FSRQ when it is core dominated and when it is lobe dominated as SSRQ (e.g., Gaur et al. (2019), and reference therein).

2. **Radio-quiet AGN**

- **Seyfert galaxies** are named after Carl Seyfert, who discovered them in 1943. Their most important characteristics are a bright, pointlike central nucleus and a spectrum showing broad emission lines. The continuous spectrum has a non thermal component, which is most prominent in the ultraviolet. The emission lines are thought to be produced in gas clouds moving close to the nucleus with large velocities. They are often associated with spiral galaxies (e.g., Karttunen (2003), and reference therein). There are two principal types, Seyfert 1 and Seyfert 2 galaxies, including several intermediate types with spectral properties between the two. In a type-1 spectrum, the allowed lines are broad (corresponding to a velocity of 10^4 kms^1), much broader than the forbidden lines. In type-2, all lines are similar and narrow with a velocity of < 10^3 km/s. Transitions between these types and intermediate cases have sometimes been observed (e.g., Karttunen (2003); Rakshit and Stalin (2017); Lakićević (2018); Chen and Yen-Chen (2019); Salvestrini (2022), and reference therein).
- **Radio-quiet quasars** do not show signs of radio jets (e.g., Barvainis (2005)). They are essentially more luminous versions of Seyfert galaxies: the distinction is arbitrary and is usually expressed in terms of a limiting optical magnitude (e.g., Dunlop (2003)).
- **Low Ionization Nuclear Emission-Line Regions (LINERs)**
  According to Heckman (1980), LINER is a type of galactic nucleus that is defined by its spectral line emission. LINERs resemble Seyfert 2 galaxies, except that the low-

ionization lines, e.g., [O I] λ 6300 and [N II] $\lambda\lambda$ 6548, 6583, are relatively strong. LINERs are the most common type of active galaxies in our local Universe. LINERs are described by optical line ratios that are not typical of photoionization by main sequence stars (e.g., Ho (2008); Cid Fernandes et al. (2011); Tommasin et al. (2012); Pović et al. (2016); Márquez et al. (2017); Cazzoli et al. (2018); Hermosa Muñoz et al. (2020)). While classical AGNs represent only a small percentage of the galaxy population, that can account for up to 50% of the total local extragalactic population (e.g., Ho et al. (2008)).

In addition, in optical, AGN can be classified as type-1 and type-2 taking into account their optical spectra and presence or absence of the broad component in emission lines, respectively (see e.g., Netzer et al. (2015) review, and references therein).

Unification model

This model consists also of SMBH in the centre as a source of all AGN power, which is surrounded by an accretion disc, BLR of high-velocity gas and NLR of lower-velocity gas, as suggested in the standard model. However, the unification model proposed that different components can be obscured by dusty torus and this is the reason for observing different types of AGN. The idea behind the unification model can be seen in figure 2.1, where depending on the absence or presence of a jet and the orientation (viewing angle) toward the observer different types of AGN can be seen, combining various central activities and various inner dust torus properties (e.g., XueGuang et al. 2022). The most significant characteristics of AGN are broad emission lines in the optical and UV bands. They aren't present in all AGN as mentioned above objects with broad lines are categorised as type-1 AGN, while objects without broad lines as type-2 AGN (e.g., Antonucci 1993). This model found however many problems with the new data being used, especially in infrared, showing that there could be also intrinsic differences in properties of different types of active galaxies, and not only the orientation effect (see Netzer et al. (2015) review for more information).

2.1.3 Standard relations

In this section, we will describe some of the main relations that characterize galaxies and that are of importance for this work.

1. **Colour-stellar mass (magnitude) diagram**

   As introduced above, in section 1, the distribution of galaxies observed in optical in the colour-stellar mass (magnitude) diagram displays two principal groups: red sequence and blue cloud galaxies (e.g., Nogueira-Cavalcante et al. 2018, and references therein). As mentioned previously, BC galaxies are actively star-forming systems and rich in gas, while RS galaxies are gas-poor and have little or no star formation. Between the RS and

the BC, there is a sparsely populated region known as the green valley, as mentioned above (e.g., Salim 2014).

Bi-modal distribution of galaxies, shown in figure 2.2, introduces RS, GV, and BC galaxies. From figure 2.2, we can see that both ET and LT galaxies traverse almost all u−r colour range, in line with other studies (e.g., Schawinski et al. (2010); Pović et al. (2013)). The GV is a well-defined location only in the all-galaxies panel. Most of the early types lie in the RS with a long tail of ∼10% to the BC at relatively low masses, this could represent blue galaxies transiting rapidly through the GV to the RS. Remarkably, the late-types form a single, unimodal distribution peaking in the blue and reaching the RS, at higher masses, with no sign of a GV (e.g., Schawinski et al. (2014)). The superposition of two distinct populations—LT, which are in the BC and smoothly decrease to the RS, and ET, a few of whose colours reach the BC—causes the bimodality in figure 2.2.

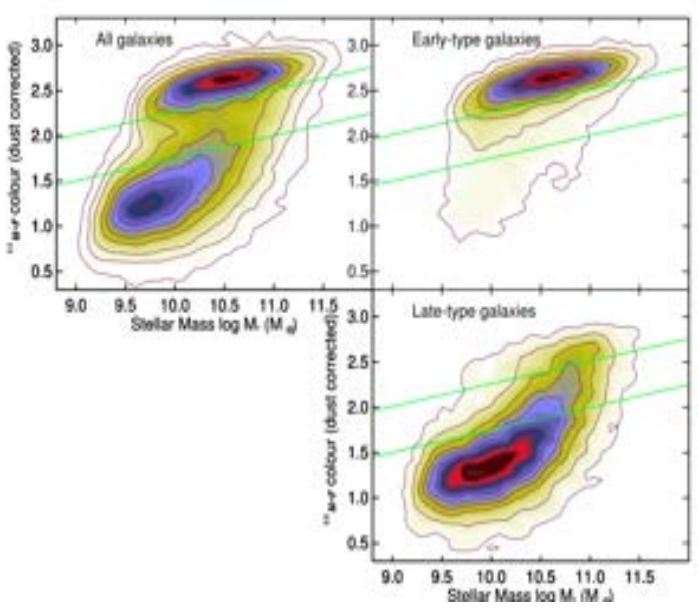

Figure 2.2: Dust corrected (u-r) colour–stellar mass diagram. The top left plot, shows all galaxies, whereas right top and bottom plots show early- and late-type galaxies, respectively, in the SDSS Galaxy-Zoo survey. Green lines show the GV. Figure is adapted from: Schawinski et al. (2014).

2. **Colour-colour diagram**

The O, B, and A stars all have different colours and lifetimes, which can be used to determine how recently galaxies formed stars. Several studies showed the high sensitivity of the UV-optical colour-colour diagram to the time derivative of the SFR, allowing us to infer that the present SFHs of the ET and LT galaxies in GV are distinct (e.g., Brammer et al. (2009); Pović et al. (2012); Pović et al. (2013); Salim (2014); Schawinski et al. (2014); Lee et al. (2015); Ge et al. (2018); Phillips et al. (2019)). It has been suggested that ET and LT galaxies have different evolutionary paths and transition timescales through the GV, from short ones < 1 Gyr to intermediate 1-2 Gyr to timescales > 2 Gyr, with ET galaxies having faster transitions (e.g., Schawinski et al. (2014), Noirot et al. (2022)). Figure 2.3 shows an example of the NUV-u versus u-r colour-colour diagrams of local galaxies. The top-left panel shows the entire galaxy population of the green valley, ET and LT galaxies. The top-right panel shows only the ET galaxies, and the bottom-right panel, show only the LT galaxies (e.g., Schawinski et al. (2014)).

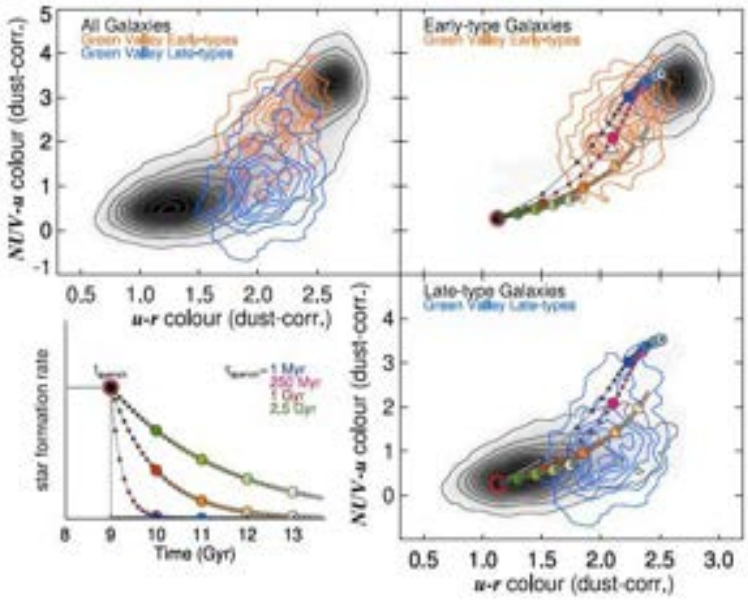

Figure 2.3: UV-optical colour-colour diagram of all (top left), ET (top right), and LT (bottom right) galaxies, which can be used to diagnose the recent star formation histories of galaxies (bottom left). Figure is adapted from: Schawinski et al. (2014).

3. **Star formation rate vs. stellar mass diagram**

The SFR vs. stellar mass diagram is one of the fundamental diagrams used to study the properties of galaxies and their evolution (e.g., Brinchmann et al. (2004); Elbaz et al. (2007); Labbé et al. (2010); Whitaker et al. (2012); Guo et al. (2013); Leslie et al. (2016); Pović et al. (2016); Netzer et al. (2016)). It has been seen at both low and high redshift, that there is a linear correlation between the SFR and stellar mass for star-forming galaxies, called the main sequence (MS) of star formation, as mentioned above. ET galaxies are found to reside, in general, below the MS, having lower SFRs and higher stellar masses. It has been suggested that the MS of SF is evolving with redshift (e.g., Whitaker et al. (2012)). Figure 2.4 below gives an example of an SFR vs. stellar mass diagram about the spectroscopic type of galaxy (Leslie et al. (2016)). The top-left to bottom-right panels include galaxies classified using the BPT-NII diagram (Kewley et al. (2006)), as purely star-forming, composite, Seyfert 2, LINER, or ambiguous, and the final panel contains all classes together. A black dashed line in each panel represents the local MS relation for star-forming galaxies. The blue contours of the star-forming galaxies are included in all panels to indicate the location of the MS. In general, composite galaxies have a higher SFR than Seyfert 2s, with LINERs having the lowest SFR (Leslie et al. (2016)).

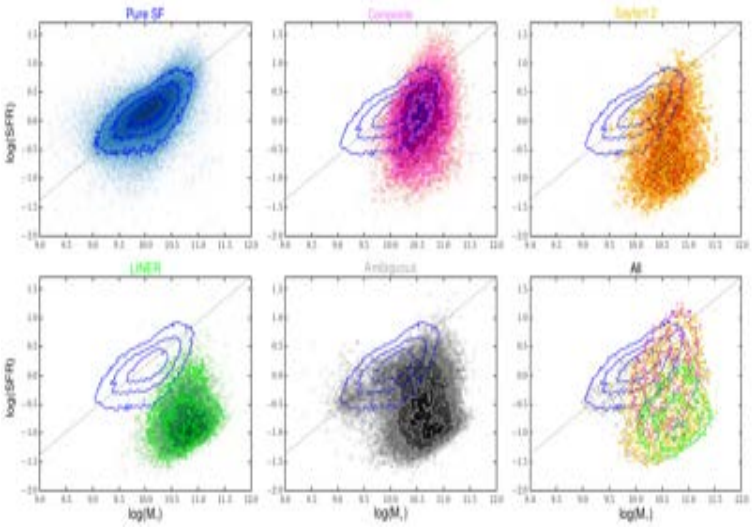

Figure 2.4: SFR as a function of stellar mass for different spectroscopic types of galaxies: star-forming (top-left), composite (top-center), Seyfert 2 (top-right), LINERs (bottom-left), ambiguous (bottom-center), and all galaxies (bottom-right). Figure is adapted from: Leslie et al. (2016).

2.2 The properties of green valley galaxies

The properties of green valley galaxies are essential for understanding the star formation quenching mechanisms, morphological transformation, and galaxy evolution across cosmic time (e.g., Salim et al. (2007); Pović et al. (2012); Pan et al. (2013); Salim et al. (2014); Schawinski (2014); Lee et al. (2015); Smethurst et al. (2015); Trayford et al. (2016); Mahoro et al. (2017); Coenda, Martínez and Muriel (2018); Ge et al. (2018); Mahoro et al. (2019); Phillips et al. (2019); Angthopo et al. (2020); Kacprzak et al. (2021); Chang et al. (2022); Mahoro et al. (2022); Noirot et al. (2022)). In the following, we summarised some of the main properties of GV galaxies.

2.2.1 Morphology and structure

There is inconsistency in previous studies regarding the morphology of GV galaxies. Different studies suggested different fractions of morphological types, with 70% - 95% being spiral galaxies and 5% – 30% ellipticals (e.g., Schawinski et al. (2014); Das et al. (2021)).

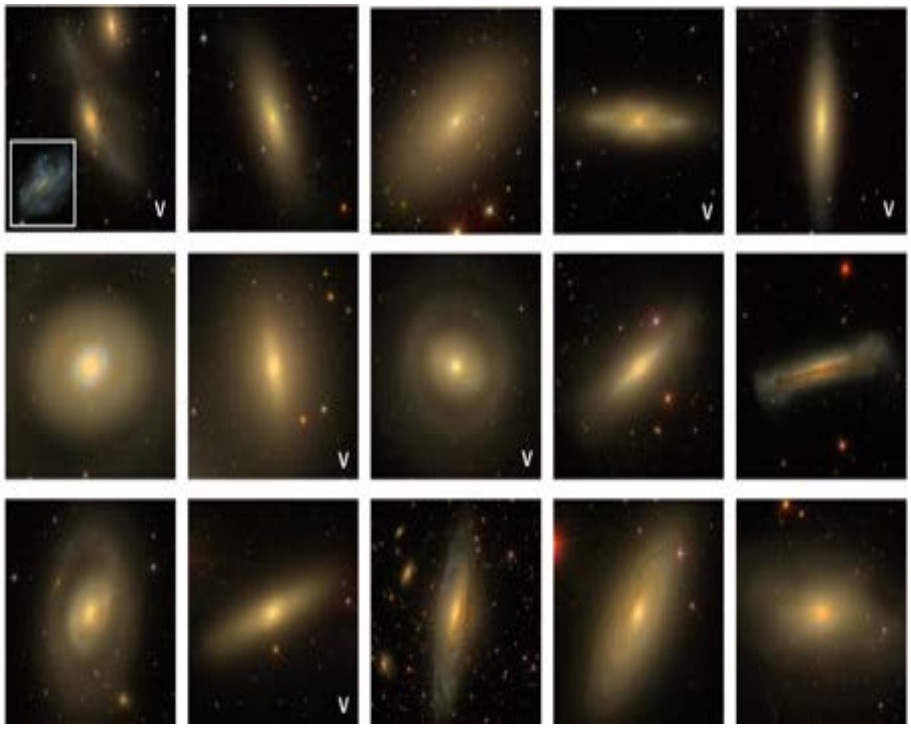

Figure 2.5: A collage of SDSS colour images of some of the nearest (D < 25Mpc) GV galaxies, spanning the mass range from log M_* = 9.3 (upper left) to log M_* = 11.4 (lower right). Figure is adapted from: Salim et al. (2014).

Figure 2.5 above illustrates an optical image of a sample for the nearest, 10 < D < 25Mpc, GV galaxies, which is observed by SDSS and GALEX selected to be distributed over a range of masses of $9.3M_{\odot} < \log M_{*} < 11.4M_{\odot}$. Most of the galaxies are neither standard like LT galaxies nor ET galaxies but are alike to be a hybrid class (e.g., Salim (2014)). The authors analysed a sample of 30 GV galaxies with deep optical imaging and FUV data from the HST and found that the rings of various shapes and sizes were common in UV but not in optical. The authors also observed that while the majority of S0s are quiescent, about 20% are in the GV. Sb galaxies, on the other hand, are primarily located in the star-forming sequence, though some do enter the GV.

2.2.2 Stellar populations in green valley

GV galaxies in many aspects, have intermediate properties between those of RS and BC galaxies in terms of stellar mass, colour, stellar populations, SFRs, or metallicity (e.g., Worthey (1994); Bruzual and Charlot (2003); Spengler et al. (2017); Liu (2020)). Stellar population studies aim to comprehend a galaxy's formation and evolution by examining properties such as stellar types, kinematics, chemical abundances, and ages, as well as determining the metallicities. Stellar populations provide some of the fundamental differences between the BC and RS galaxies, with, on average, older stellar populations dominating the RS and younger the BC, as mentioned previously (e.g., Kauffmann et al. (2003)). Other studies show that GV galaxies are older compared to BC and younger compared to RS (e.g., Pan et al. (2013)). Figure 2.6 shows (from top to bottom), trends with velocity dispersion of average stellar age, pseudo-quenching time-scale, metallicity and extinction. The left and right panels show the Dn4000- and colour-based GV sample selections, respectively. The blue dashed, green dotted, and red solid lines represent three different GV samples. The figure further demonstrates the consistency of the monotonically decreasing trend of dust attenuation with σ. It also depicts a distinct stratification from lGV to uGV, with mGV galaxies having properties that are more similar to lGV galaxies.

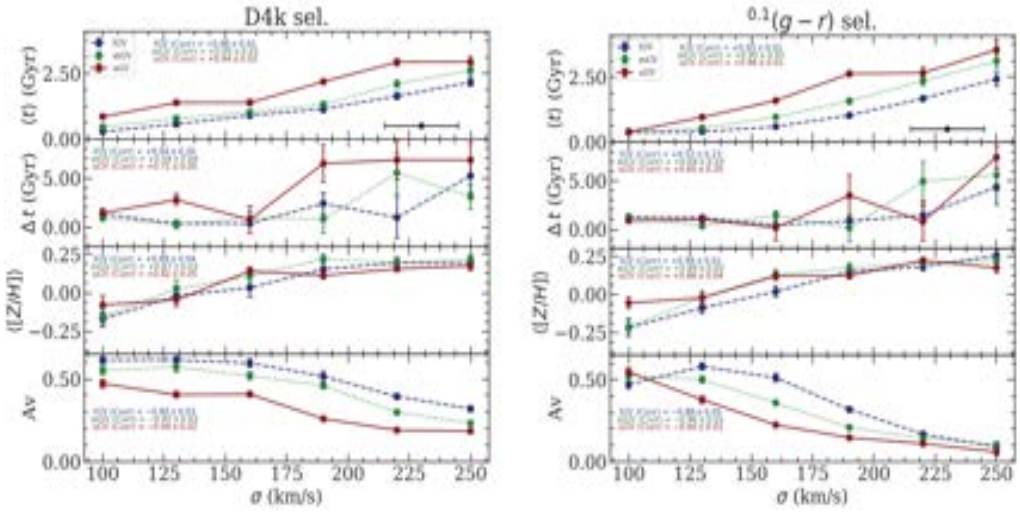

Figure 2.6: From top to bottom: average stellar age, pseudo- quenching time-scale, metallicity and dust attenuation as a function of velocity dispersion for GV galaxies selected using the Dn4000 (left) and colour (right) criteria. Figure is adopted from Angthopo et al. (2020).

2.2.3 Environment and clustering

It is widely known that the environment has a significant role in galaxy evolution and formation. The well-known morphology-density relationship in galaxy clusters, which states that early-type galaxies and morphologically undisturbed galaxies are typically found in high-density environments and vice versa, is the best indicator of its influence (e.g., Schawinski et al. (2014); Jian et al. (2020); Das et al. (2021), and the reference therein). The impact of the environment increases as galaxy mass decreases. However, inconsistent results have been found in previous studies regarding the environment of GV galaxies, suggesting from strong through mild to no environmental dependence (e.g., Coenda et al. (2018); Jian et al. (2020); Das et al. (2021)).

Some of the previous works suggested that:

1. Slow star formation quenching mechanisms are operating in denser environments.
2. GV fraction is higher in the field but decreases with increasing M^*.
3. Effective GV fraction is lower for field galaxies of a strong mass effect.

2.2.4 Active galactic nuclei

Different X-ray and optical studies suggested that the majority of active galaxies are located in the green valley and may be responsible for star-formation quenching (e.g., Sanchez et al. 2004; Nandra et al. (2007); Salim et al. (2007); Georgakakis et al. (2008); Silverman et al. (2008); Treister et al. (2009); Hickox et al. (2009); Cardamone et al. (2010); Pović et al. (2012); Salim (2014); Mahoro et al. (2017, 2019)). In addition, some studies also suggested a connection between SF quenching and the strength of AGN, observing an anti-correlation between AGN strength and the rate of quenching (e.g., Leslie et al. (2016)). Salim et al. (2007) further studied this by selecting a sample of AGN and non-AGN through the BPT diagrams at the same stellar mass and found that AGN, peak in the star-forming sequence with the tail towards the GV being occupied by strong AGN with $L[OIII] > 10^7 L_{\odot}$ and the weak AGN occupying a lower part of the SF sequence, as showed in figure 2.7. It has been suggested that AGN is responsible for a gradual suppression of SF of galaxies. Figure 2.7 describes the relationship between the specific SFR and mass for SF and AGN galaxies. Strong AGN lies in the massive continuation of the SF sequence, with SFRs as high as those of the massive galaxies of the SF class. Higher masses with similar SFRs cause their specific SFRs to take more intermediate values. Weak AGN fall at lower SFRs relative to the strong AGN, with a tail toward low SFRs, extends well into the domain of the inactive galaxies (e.g., Salim (2014)).

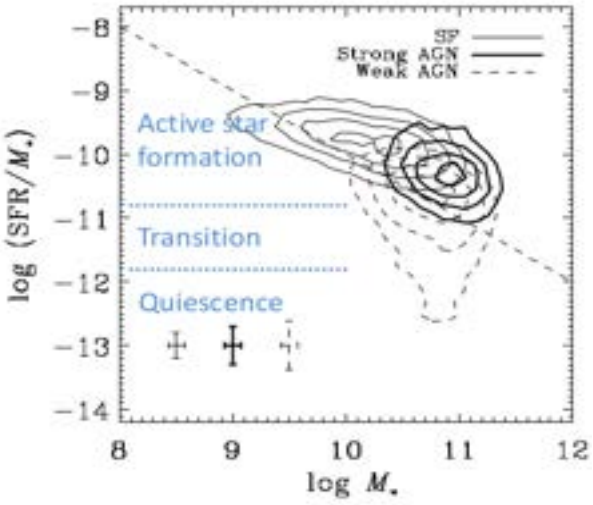

Figure 2.7: Specific SFR vs. stellar mass diagram showing the location of galaxies selected from the BPT diagram to be star-forming, strong, and weak AGN. figure is adapted from: Salim et al. (2007).

Most AGN studies in the GV showed to be more common to type-2 AGN, whose central engine is not strong enough to affect the global colour of the host. The vast majority of AGN

belong to type-2, including a large number of LINERs that not necessarily are photoionised by AGN (Cid Fernandes et al. (2004, 2011)). Type-1 AGN have broad emission lines and contribute to continuum emission (e.g., Salim (2014)). Trump et al. (2013) omitted the central sources of broad-line AGN to study host colours and found that such AGN are mainly located in optically bluer hosts, which is in line with the results for luminous type-2 AGN.

2.3 The role of AGN in star formation quenching in the green valley and galaxy evolution

Several methods were studied and proposed as responsible for SF quenching and galaxy transformation, including AGN negative feedback, environmental effects, thermal evaporation, starvation, strangulation, cluster interactions, galaxy minor and major mergers, supernovae winds, and secular evolution (e.g., Gunn & Gott, (1972); Cowie & Songaila, (1977); Caldwell, Larson & Tinsley, (1980); Shioya et al. (2002); Fang et al. (2013); Coenda et al. (2018); Jian et al. (2020); Das et al. (2021)). Most of the X-ray detected AGN lie in the GV, suggesting that the AGN feedback mechanism might play an essential role in SF quenching and galaxies moving from the BC to RS (e.g., Nandra et al. (2007); Povic et al. (2012)). Nevertheless, in some studies, there was no strong evidence for AGN host galaxies of having either highly suppressed or elevated SF compared to galaxies of similar stellar masses and redshift (e.g., Mateos et al. (2017)).

In Mahoro et al. (2017) the authors went a step further and analysed the importance of AGN in SF quenching by using a sample of GV X-ray detected active and non-active galaxies with far-infrared (FIR) emission. The authors measured the SFRs using FIR luminosity and different templates for active and non-active galaxies. They found that majority of active galaxies are on or above the MS of star formation, having higher SFRs in comparison to non-active galaxies within the same stellar-mass range, in contrast with previous optical studies. The same result has been obtained independently on the morphology (see Mahoro et al. (2019)). In addition, the authors studied the stellar populations of a small ($\sim$ 10%) sub-sample of AGN and non-AGN galaxies (Mahoro et al. (2022)). The authors found out that both FIR AGN and non-AGN GV galaxies are dominated by intermediate and old stellar populations, where FIR AGN have a slightly higher fraction of intermediate stellar population in comparison to non-AGN (67% versus 53%, respectively) and a lower fraction of old stellar population (23% versus 36%, respectively). However, it is still not clear what type of AGN are the galaxies in the analysed sample. Understanding better this through the X-ray and radio data is the main aim of this MSc thesis.

Chapter 3

Data and Methodology

In this work, we will use the data from the COSMOS field and a sample of active galaxies selected in Mahoro et al. (2017, 2019, 2022) to understand better the type of AGN and the role of AGN in galaxy evolution through their X-ray and radio properties. A sample selection and the data to be used are briefly described below.

The COSMOS is a deep multi-band survey centred at (RA, DEC) = (+150.1192, +2.2058), covering an area of 2 deg^2. It is designed to probe the correlated evolution of galaxies, star formation, AGN, and dark matter with large-scale structure over the redshift range 0.5 to 6 (Scoville et al. (2007)). COSMOS is the most comprehensive field that has been observed by the Hubble Space Telescope (HST) so far. Furthermore, COSMOS ensures full spectral coverage with multi-wavelength imaging and spectroscopy from X-ray to radio wavelengths by the major ground and space-based telescopes (e.g., HST, XMM, Chandra, GALEX, Spitzer, Herschel, NuStar) (Scoville et al. (2007)).

3.1 Sample selection using optical and FIR data

Since this work is based on the previous work of Mahoro et al. (2017, 2019, 2022), in this section, we will briefly describe some of the public catalogues that have been used by authors. For galaxy selection, they used the morphological catalogue of Tasca et al. (2009), based on the HST/ASC photometric data of Leauthaud et al. (2007). The catalogue contains the morphological classification of 237,912 galaxies and it is complete down to a magnitude of (I_{AB}) = 23.0 (Mahoro et al. (2017)). In addition, FIR Herschel/PACS (Poglitsch et al. (2010)) data have been used at 100m and 160m as part of the PACS Evolutional Probe (PEP, Lutz et al. (2011)) survey, for measuring the IR luminosity and SFRs. The authors also used the 24 μm IR catalogue of Spitzer for obtaining the integrated IR luminosity (Mahoro et al. (2017)). In addition, the authors used also the X-ray catalogues, mainly for a selection of AGN sources. In particular, two catalogues have been used, Chandra (Civano et al. (2012)) and XMM-

Netwon (Brusa et al. (2007)). To select AGN, the authors used the flux ratio between the hard X-rays (2 - 10 keV) and optical I band: $\log[F_x/F_0] = \log F_x + F_0/2.5 + 5.325$, and selected as AGN all sources with $-1 \leq \log F_x/F_0 \leq 1$ (e.g., Alexander et al. (2001); Bauer et al. (2004); Bundy, Ellis & Treu (2007); Trump et al. (2009)). They obtained a final sample of 1472 AGN. This is the catalogue that we used in our work as well. This sample has been divided into BC, GV, and RS sub-samples, as described in chapter 4. More information on X-ray catalogues is given below, in more detail, since they will be used also in this work.

3.2 X-ray data

3.2.1 Chandra

Chandra[1] is a flagship-class X-ray space telescope launched in July 23, 1999. Chandra's survey of the COSMOS field used a total of 4.6 Ms of exposure time (Civano et al. (2016)). Some of the last data include 56 overlapping observations with uniform coverage of $\sim$ 160ks over the whole Hubble-covered area (Civano et al. (2016)). In Mahoro et al. (2017), the authors used the Chandra catalogue of Civano et al. (2012) with 1761 X-ray sources with optical counterparts, within the central 0.9 deg of the COSMOS field down to limiting flux of $7.3 \times 10^{-16} ergcm^2 s^{-1}$ in the 2 -10 keV band. These data will be used in this work as well.

We cross-matched the optical and Chandra X-ray catalogue for finding the counterparts between the two catalogues, for a sample of AGN. We used the above-mentioned AGN catalogue of 1472 sources and cross-matched it with the Chandra catalogue of 4016 sources (Civano et al. (2016)). To find the best cross-matching radius, we first did a test and cross-matched the two catalogues using the radius from 1 to 5 arcsec, using both the best (selecting only the closest X-ray counterparts) and all cross-match. Figure 3.1 shows the number of obtained counterparts for each cross-matching radius. As a compromise between not losing sources and minimising the spurious counterparts, we selected a radius of 2 arcsec as the best one to cross-match the two catalogues. We found in total of 1297 counterparts between the AGN catalogue and Chandra X-ray data (or 88% of our total AGN sample). With this, for our AGN we obtained X-ray information, such as the X-ray flux in different bands, including 0.5 - 2 keV, 2 -10 keV, and total 0.5 - 10 keV. These data will be used in our analysis in chapter 4.

[1] https://chandra.harvard.edu/about/

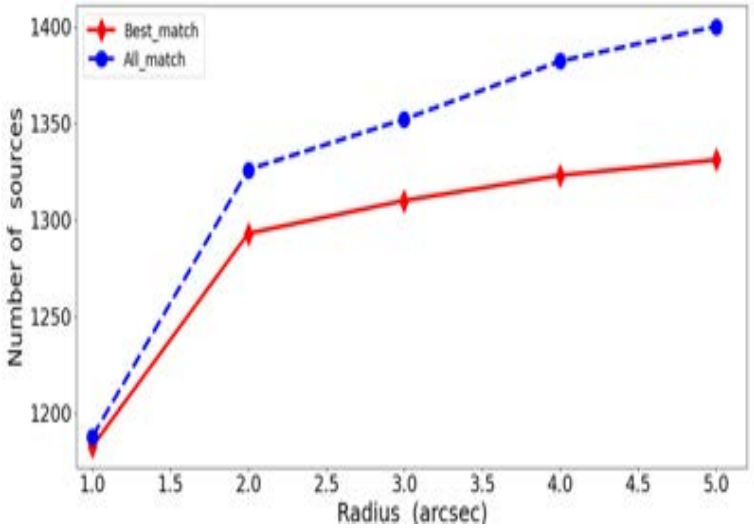

Figure 3.1: The number of best (red symbols and red solid line) and all (blue symbols and blue dashed line) counterparts for different cross-matching radius (1 -5 arcsec) when combining optical AGN and X-ray Chandra catalogues.

3.2.2 XMM-*Newton*

XMM-*Newton*[2] is an X-ray space observatory launched by the ESA in December 1999. The first homogeneous coverage in the X-rays of the whole COSMOS field was obtained with the XMM-*Newton* satellite during 1.5 Ms of exposure time (Hasinger et al. (2007); Brusa, Cappelluti and Hasinger et al. (2007)). These observations have been crucial for characterising the most luminous AGN in COSMOS (Civano et al. (2012)). In general, XMM-*Newton* detected 1800 X-ray sources down to limiting fluxes of 5×10^{-16}, 3×10^{-15}, and $7\times10^{-15} ergcm^{-2}s^{-1}$ in the 0.5 - 2 keV, 2 -10 keV and 5 -10 keV bands, respectively, over 50% of the covered area (Brusa et al. (2007)). In this work, after extracting X-ray sources from Chandra catalogue, XMM-*Newton* will be used for extraction of additional sources using Brusa et al. (2007) COSMOS catalogue of 1887 sources in total.

Similar to the case of cross-matching optical and Chandra catalogues, we went through the same exercise in the case of optical AGN and XMM catalogues, testing again the cross-matching radius of 1 - 5 arcsec. The obtained number of sources for each radius and both best- and all-match is shown in figure 3.2. As the best compromise, we selected a radius of 2 arcsec, and obtained a total of 685 counterparts (or 47% of all AGN).

[2] https://sci.esa.int/web/xmm-newton/-/31249-summary

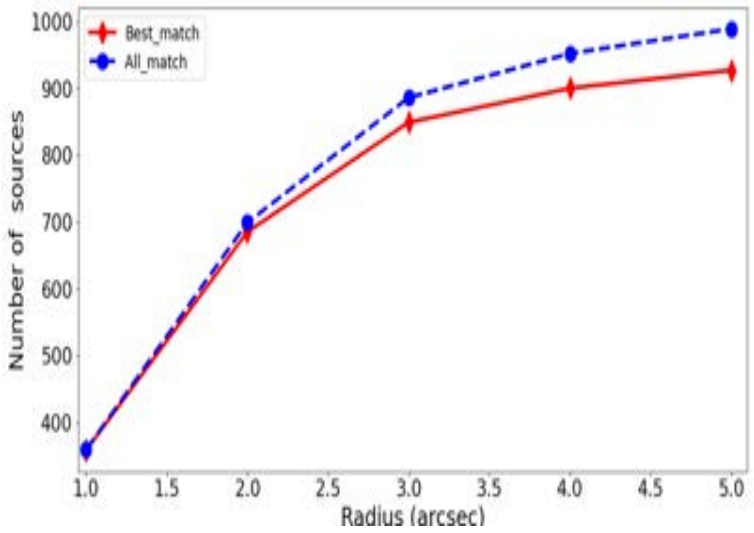

Figure 3.2: The number of best (red symbols and red solid line) and all (blue symbols and blue dashed line) matched sources for different cross-matching radius (1 -5 arcsec) when combining optical AGN and XMM-*Newton* catalogues.

3.3 Radio data

3.3.1 The Very Large Array (VLA)

The VLA[3] is the most versatile, widely-used radio telescope in the centimetre regime. It can map the large-scale structure of gas and molecular clouds and pinpoint ejections of plasma from SMBH. Some of the principal and most used VLA surveys are the FIRST and NVSS. The FIRST (Faint Images of the Radio Sky at Twenty-cm)[4] VLA radio survey began in 1993 (Helfand et al. (2015)). The FIRST survey provides images and data for almost 1 million sources, covering a total of $\sim$ 10600 deg^2 largely coincident with the SDSS area, with 35% of sources having resolved structure on scales from 2-30" (Helfand et al. (2015)). Approximately 30% of observed FIRST radio sources have optical SDSS counterparts. The NVSS (NRAO VLA Sky Survey) [5] is a 1.4 GHz (21cm) continuum survey covering the entire sky north of -40° declination with an angular resolution of 45 arcsec. The images are insensitive to smooth radio structures larger than several arcminutes in both coordinates. In this work, we used the FIRST and NVSS data only as support, checking on the availability of images for performing a visual classification of radio morphology. However, due to the higher redshift of our AGN sample (z > 0.5 in most cases), we obtained the FIRST and NVSS images for an insignificant

[3] https://public.nrao.edu/telescopes/vla/
[4] https://public.nrao.edu/telescopes/vla/
[5] https://www.cv.nrao.edu/nvss/

number of sources only, and therefore we didn't go through any important analysis using these data. The VLA-COSMOS Large Project has imaged the 2 deg^2 of the COSMOS field with a resolution of 1.5 arcsec and a sensitivity of about 11Jy giving a catalogue of $\sim$ 3600 radio sources (Bondi et al. (2008)). In this work, we used the VLA-COSMOS catalogues to extract radio morphology and different radio properties of our selected AGN sample. We will study the radio fluxes and luminosity, particularly at 1.4GHz, to determine whether our sources are radio loud or quiet.

One of the principal radio catalogues used in this work is the VLA-COSMOS Large project catalogue at 1.4 GHz presented by (Schinnerer et al. (2010)). This catalogue has a total of 3601 sources. Taking into account previous studies and lower resolution in radio, to cross-match our AGN catalogue with this catalogue, we used 5 arcsec radius and best-match. We obtained in total 227 AGN with radio counterparts in Schinnerer et al. (2010) 1.4 GHz catalogue (15% of our AGN sample). After this cross-matching, we can obtain the peak flux density and integrated flux density at 1.4 GHz of all counterparts. Finally, we crossed-matched our AGN catalogue with the 3GHz radio catalogue of Smolčić et al. (2017) with 2865 sources in total. We used again the cross-matching radius of 5 arcsec for cross-matching. We found a total of 535 counterparts between the two catalogues (36% of our AGN sample). From the 3GHz radio catalogue, we can extract the radio flux and luminosity at 3GHz. In addition, 21cm luminosity is also available and will be used in our analysis in chapter 4. From the same catalogue we were able to extract the SFR measured using the IR data after integrating the whole IR range of 8 - 1000 μm and obtaining the total IR luminosity (Smolčić et al. (2017)). Finally, out of all 3GHz counterparts, 9% of sources (137 in total) have radio classification available in Vardoulaki et al. (2021) catalogue, which we also used in our analysis in chapter 4.

3.4 Summary of all used data

To summarise, in this work we used the optical, X-ray, and radio data of a sample of AGN from the COSMOS survey. We started with a sample of 1472 AGN selected in Mahoro et al. (2017) using optical and X-ray data. Using a cross-matched radius of 2 arcsec, we cross-matched the AGN sample with the X-ray Chandra and XMM-*Newton* data, and 1.4 GHz and 3 GHz radio data, obtaining in total 1297, 685, 227, and 535 counterparts, respectively. Figure 3.3 shows the distribution of all AGN with available multiwavelength data. In total, we found a total of 1472 new pairs of sources. Figure 3.3 also shows the right ascension (RA) versus declination (DEC) for Chandra, VLA, and XMM-*Newton*.

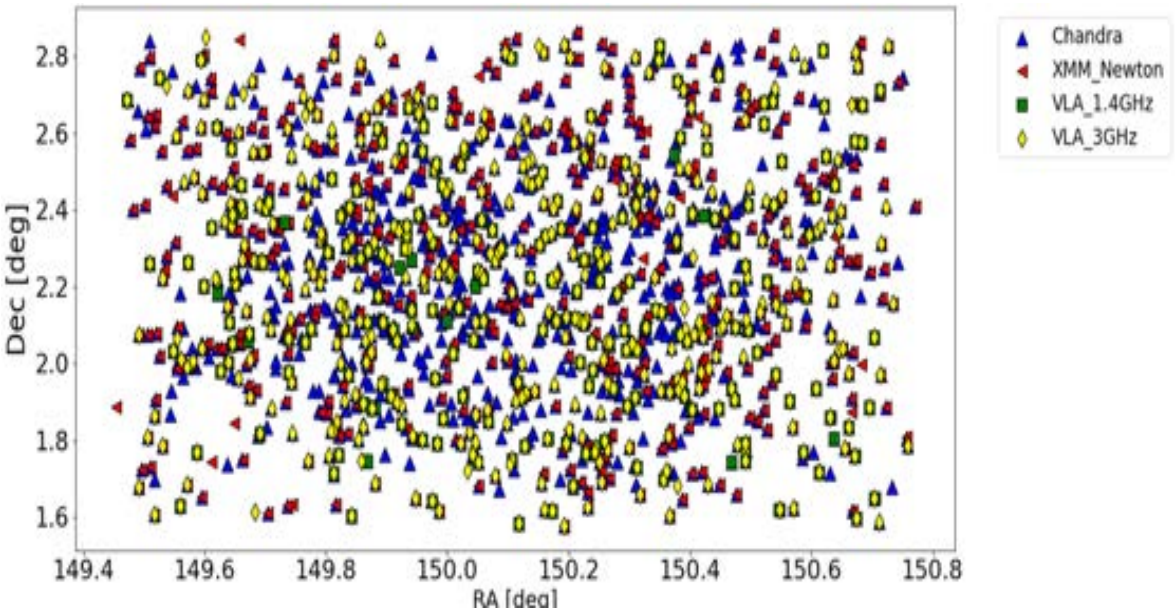

Figure 3.3: Distribution of all AGN studied in this work with available multiwavelength data in X-rays with Chandra (blue top oriented triangles) and XMM-*Newton* (red left oriented triangles), and in radio at 1.4 GHz (green squares) and 3 GHz (yellow diamonds).

Chapter 4

Analysis

In this chapter, we describe all analysis carried out using the sample of AGN and multiwavelength data described in chapter 3. We first studied the properties of galaxies in the BC, GV, and RS in optical, then in X-rays, and finally in radio. Across all analysis, we used the median values of parameters distributions, together with the lower quartile (Q1, covering 25% of the sample) and upper quartile (Q3, covering 75% of the sample), to compare the distributions of different parameters of BC, GV, and RS AGN. These statistics are given in table 4.1 for all analysed parameters of BC, GV, and RS AGN.

Table 4.1: Statistical summary of analysed parameters in optical.

BC AGN			
No	Analysed parameter	Q1 – Q3	Median
1	U-B rest-frame colour	0.51 – 0.74	0.65
2	Redshift	0.74 – 1.48	1.23
3	log(M_*) [$M_\odot$]	10.01 – 10.87	10.59
4	Absolute magnitude in B-band	-22.30 – -20.60	-21.53
5	Absolute magnitude in F814W band	-23.05 – -21.30	-22.31

GV AGN			
No	Analysed parameter	Q1 – Q3	Median
1	U-B rest-frame colour	0.88 – 1.07	0.97
2	Redshift	0.75 – 1.54	1.00
3	log(M_*) [$M_\odot$]	10.45 – 10.95	10.73
4	Absolute magnitude in B-band	-22.14 – -20.73	-21.50
5	Absolute magnitude in F814W band	-22.95 – -21.70	-22.40

RS AGN			
No	Analysed parameter	Q1 – Q3	Median
1	U-B rest-frame colour	1.26 – 1.58	1.40
2	Redshift	0.81 – 2.50	1.08
3	log(M_*) [$M_\odot$]	10.60 – 11.13	10.86
4	Absolute magnitude in B-band	-23.34 – -20.75	-21.67
5	Absolute magnitude in F814W-band	-23.74 – -21.87	-22.70

4.1 Sample characterisation in optical

In this section, we compare the properties of BC, GV, and RS AGN such as the U-B rest-frame colour, redshift, stellar mass, and absolute magnitude in B and F814W bands. All parameters have been extracted from the initial AGN catalogue of Mahoro et al. (2017).

4.1.1 U-B rest-frame distribution of AGN

Previous studies showed that the distribution of all galaxies and the limit that corresponds to the GV selection if using U-B rest-frame colours is $0.8 \leq$ U-B ≤ 1.2 (e.g., Willmer et al. (2006); Nandra et al. (2007)) for a similar redshift as in Mahoro et al. (2017). Using this criteria, in Mahoro et al. (2017) the authors selected a total of 317 and 13877 AGN and non-AGN GV galaxies, respectively with FIR counterparts. In our work, we used the same criteria to separate the BC, GV, and RS AGN as follows:

$$0 \leq \text{U-B} \leq, 0.8, \text{ for selecting BC AGN}$$

$$0.8 < \text{U-B} \leq 1.2, \text{ for selecting GV AGN, and}$$

$$\text{U-B} > 1.2, \text{ selecting RS AGN.}$$

Figure 4.1 shows the distribution of U-B rest-frame colour of AGN sample and separation of the sample into the BC, GV, and RS, as mentioned above. In total, we have 522 (35%), 606 (41%), and 292 (20%) sources in the BC, GV, and RS, respectively, out of the total sample of AGN. Out of 1472 AGN, 52 sources (4%) remain out of the criteria used above for selecting BC, GV, and RS galaxies, and remain as 'outliers'. We can see that the highest fraction of AGN is located in the GV, followed by the BC, and finally RS. This is in line with previous works who suggested that most of the X-ray detected AGN are located in the GV (e.g., Nandra et al. (2007); Pović et al. (2012)).

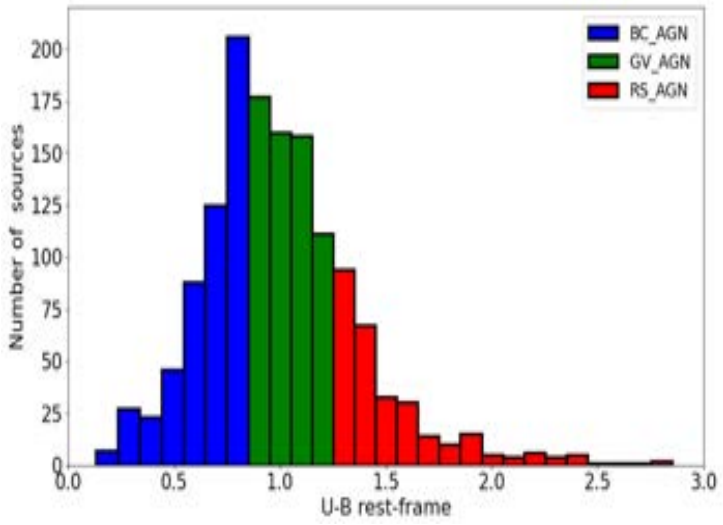

Figure 4.1: Rest-frame U-B colour distribution of the total sample of COSMOS active galaxies. Samples of BC, GV, and RS AGN are marked with blue, green, and red colours, respectively.

4.1.2 Redshift distribution

In this section, we analysed the redshift distribution of selected BC, GV, and RS AGN. We extracted the photometric redshifts from Salvato et al. (2011) catalogue, measured using the LePhare code (Arnouts & Ilbert (2011)) with 30 photometric bands down to a magnitude of $I_{AB} = 25$ and using AGN templates. Photometric redshift distribution of BC, GV, and RS AGN is shown in figure 4.2 (in blue solid, green dot-dashed, and red dashed lines, respectively). On average, all three groups have similar redshift distribution. BC AGN is on average at a bit larger redshift, with a median value of 1.23, in comparison to GV and RS AGN whose median redshift is 1.0 and 1.08, respectively. However, 50% of both BC and GV occupy the same region of $\sim$ 0.75 - 1.5 (or 0.74 - 1.48 and 0.75 - 1.54, respectively). RS AGN has a broader range in redshift, due to a larger number of galaxies at higher redshifts (around $z \sim 3$) in comparison to both BC and GV. These galaxies at larger redshift shall be further checked in the future for confirming their type and properties.

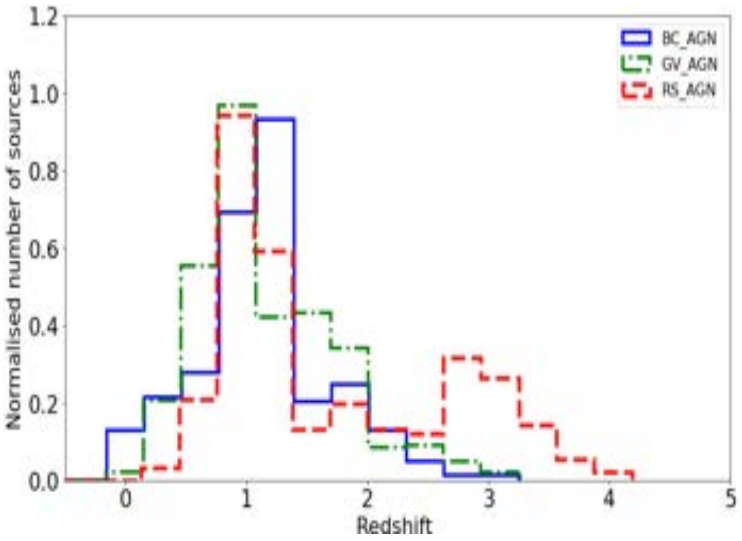

Figure 4.2: The normalised redshift distribution of BC, GV, and RS AGN as indicated in the label.

4.1.3 Stellar-mass distribution

In this section, we analysed the stellar mass distribution of the BC, GV, and RS AGN. Stellar masses were extracted from Mahoro et al. (2017) catalogue. They were measured through SED fitting, using the KCORRECT code Blanton & Roweis (2007), the photometric information from 10 optical/NIR bands, $\sim$ 500 spectral templates (Blanton & Roweis (2007), and Salpeter IMF (Salpeter (1955)). The distribution of the stellar mass is shown in figure 4.3. BC AGN, on average, shows slightly lower stellar mass, with the median value of logM* = 10.59 $M_{\odot}$, in comparison to median stellar masses of GV and RS AGN of logM* = 10.73 $M_{\odot}$ and 10.86 $M_{\odot}$, respectively. Similarly, 50% of BC, GV, and RS AGN occupy the stellar mass range of logM* = 10.01 - 10.87 $M_{\odot}$, 10.45 - 10.95 $M_{\odot}$, and 10.60 - 11.13 $M_{\odot}$, respectively. This is in line with the previous results that studied a large sample of galaxies in general (not only active galaxies), showing that RS galaxies on average have larger stellar masses at both lower (e.g., Schawinski et al. (2014)) and higher (e.g., Pović et al. (2013)) redshifts.

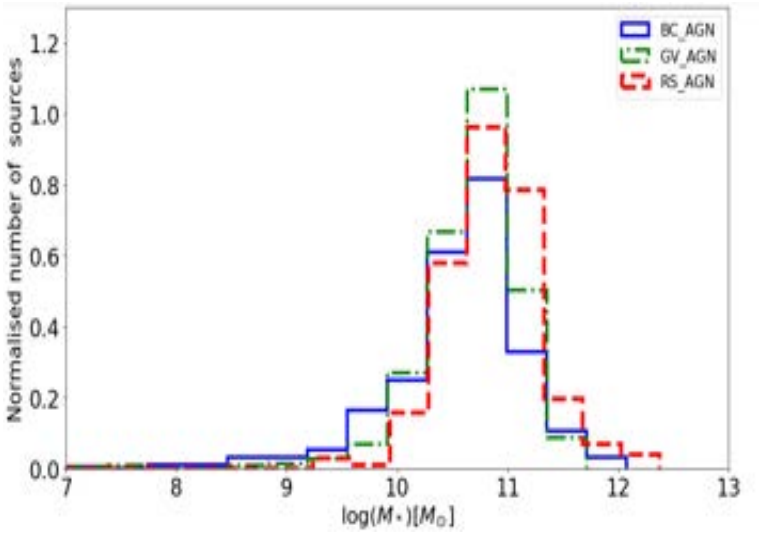

Figure 4.3: The normalised stellar mass (log(M_*) [$M_\odot$]) distribution of BC, GV, and RS AGN as indicated in the labels.

4.1.4 Absolute-magnitude distribution

We analysed the distribution of the absolute magnitude of BC, GV, and RS AGN, as can be seen in figure 4.4. We selected two photometric bands, B in the blue part of the spectrum and F814W in the red part. Absolute magnitudes have been extracted from Mahoro et al. (2017) catalogue. They were measured using the K-corrected magnitudes, after obtaining the K-correction with the KCORRECT code (Blanton & Roweis (2007)). For more information see Mahoro et al. (2017), and references therein. As can be seen in figure 4.4 and table 4.1, BC, GV, and RS AGN show similar intrinsic brightness in both analysed bands, with RS being slightly brighter, as expected taking into account the previous finding that they are also slightly more massive. Median B-band (F814W) absolute magnitude of RS AGN is -21.67 (-22.70) in comparison to -21.53 (-22.31) and -21.50 (-22.40) of BC and GV AGN, respectively. This is again in line with previous results, although these results show smaller differences than when dealing with non-active galaxies (e.g., Pović et al. (2012), (2013); Schawinski et al. (2014)).

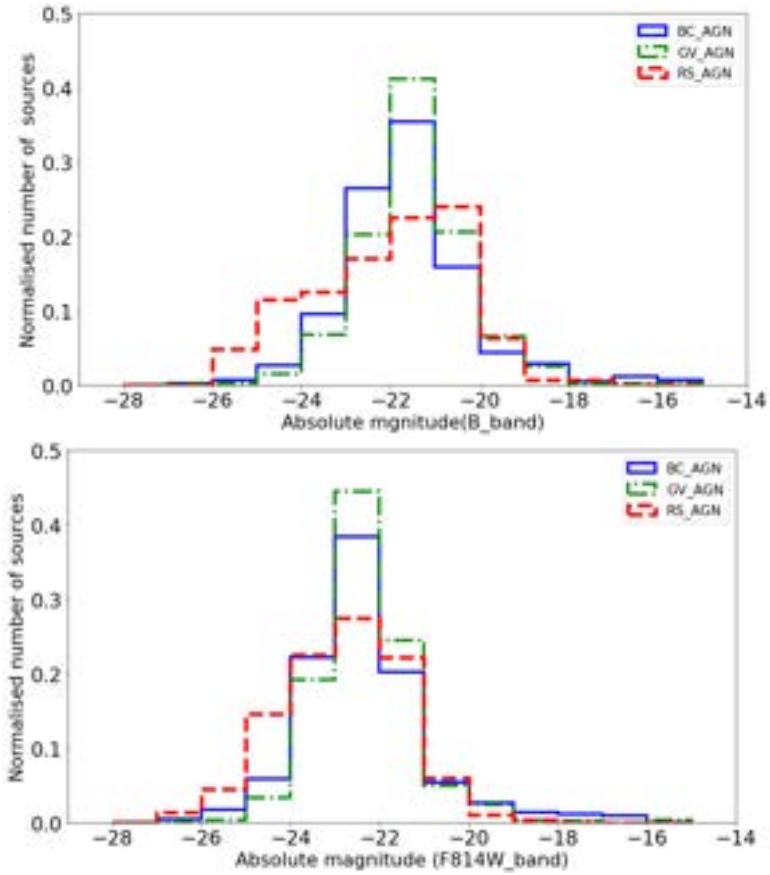

Figure 4.4: Normalised distribution of B-band (top) and F814W-band (bottom) absolute magnitude of BC, GV, and RS AGN, as indicated in the labels.

4.2 X-ray analysis

In this section, we focused on the analysis of X-ray properties of BC, GV, and RS AGN, using the information provided in both Chandra and XMM-*Newton* catalogues. We analysed several properties using different X-ray bands, such as the X-ray-to-optical flux-ratio, X-ray-colours, and X-ray luminosity distribution. These statistics are given in tables 4.2 and 4.3 obtained using Chandra and XMM-*Newton* data, respectively.

Table 4.2: Statistical summary of analysed parameters in Chandra.

BC AGN			
No	Analysed parameter	Q1 – Q3	Median
1	logL_x (0.5 - 2 keV)	42.75 – 43.59	43.17
2	logL_x (2 - 10 keV)	43.47 – 44.09	43.81
3	logL_x (0.5 - 10 keV)	43.35 – 44.18	43.78
4	HR3	-0.35 – 0.17	-0.15

GV AGN			
No	Analysed parameter	Q1 – Q3	Median
1	logL_x (0.5 - 2 keV)	42.45 – 43.31	42.89
2	logL_x (2 - 10 keV)	43.20 – 43.91	43.57
3	logL_x (0.5 - 10 keV)	43.12 – 43.92	43.53
4	HR3	-0.24 – 0.30	-0.03

RS AGN			
No	Analysed parameter	Q1 – Q3	Median
1	logL_x (0.5 - 2 keV)	42.38 – 43.65	42.95
2	logL_x (2 - 10 keV)	43.19 – 44.27	43.64
3	logL_x (0.5 - 10 keV)	43.03 – 44.25	43.61
4	HR3	-0.26 – 0.31	0.01

Table 4.3: Statistical summary of analysed parameters in XMM-*Newton*.

BC AGN			
No	Analysed parameter	Q1 – Q3	Median
1	logL_x (5 - 10 keV)	43.54 – 44.26	43.96
2	log(X/O)	-0.13 – 0.47	0.24
3	HR1	-0.60 – -0.28	-0.52
4	HR2	-0.49 – -0.14	-0.39

GV AGN			
No	Analysed parameter	Q1 – Q3	Median
1	logL_x (5 - 10 keV)	43.14 – 44.09	43.65
2	log(X/O)	-0.12 – 0.62	0.24
3	HR1	-0.54 – 0.05	-0.35
4	HR2	-0.38 – 0.03	-0.23

RS AGN			
No	Analysed parameter	Q1 – Q3	Median
1	logL_x (5 - 10 keV)	43.31 – 44.69	43.73
2	log(X/O)	-0.04 – 0.79	0.59
3	HR1	-0.47 – -0.08	-0.32
4	HR2	-0.34 – 0.06	-0.16

4.2.1 X-ray-to-optical flux ratio (X/O) distribution

X-ray-to-optical flux ratio showed to be important for characterising the amount of X-ray emission in celestial sources and their classification (e.g., Della Ceca et al. (2004); Pović et al. (2009a,b)). It is defined as the ratio between the flux in X-rays and the flux in optical. X/O flux ratio provides some of the easiest ways to classify the nuclear type. The typical value of log(X/O) flux ratios for X-ray selected AGN is in the range between -1 and 1 (e.g., Alexander et al. (2001); Fiore et al. (2003); Della Ceca et al. (2004)). At higher X/O flux ratios we can find broad- and narrow-line AGN, high-redshift obscured AGN (type 2 QSOs), high-redshift clusters of galaxies, and blazars. The region with $\log(X/O) < 0.1$ is typically populated by coronal emitting stars, normal galaxies (both early- and late-types) and nearby heavily absorbed (Compton thick) AGN. In this work, for defining X/O flux ratio, we used similar bands and definition as in Pović et al. (2009a,b). In X-rays, due to the lack of 0.5 - 4.5 keV band, we used as an approximation the XMM-*Newton* fluxes in the range of 0.5 - 5 keV, measured using fluxes in three other available bands, 0.5 - 2 keV, 2 - 10 keV, and 5 - 10 keV, as:

$$F(0.5-5kev) = F(0.5-2keV) + F(2-10keV) - F(5-10keV) \tag{4.1}$$

All X-ray fluxes have been K-corrected, following the work of Ptak et al. (2007) and using equation:

$$F_{X,Kcor} = (1+z)^{\Gamma-2} \times F_{X,obs} \tag{4.2}$$

where Fx, kcor indicates the K-corrected X-ray flux, z is the redshift, Γ denotes the gamma constant for which we used a value of 1.9, and Fx,obs is the observed X-ray flux in a particular X-ray band. The K-correction is used to convert astronomical object measurements into their respective rest frames. In optical, we used the K-corrections and K-corrected magnitudes from Mahoro et al. (2017) paper, as described above. We first measured the flux density in R band, using the standard equation for AB mag-flux density relation:

$$m_{AB} = -2.5 \log_{10} f_\nu - 48.60. \tag{4.3}$$

The flux density is then measured as:

$$f_\nu = 10^{\frac{m_{AB}+48.60}{-2.5}}. \tag{4.4}$$

Using the equation $f \times \lambda$=c and the central wavelength of the used R Subaru filter of 6288.71 Å, we then converted from the flux density to flux in [erg/sec/cm^2]. We then calculated the flux optical as $F_{opt} = f_\nu \times f$. Finally, X/O flux ratio was measured using the K-corrected fluxes in both X-rays and optical in R band as:

$$X/O = \log\left(\frac{F_x(0.5-5keV)}{F_{opt}}\right) \tag{4.5}$$

We measured X/O flux ratio only for those sources that have X-ray flux available in all 3 bands, as indicated in equation 4.1, selecting in total 92 (7%) sources out of the total sample of AGN. Out of this, 36 (2%), 41 (3%), and 15 (1%) are BC, GV, and RS AGN, respectively. Figure 4.5 shows the distribution of the X/O flux ratio of BC, GV, and RS AGN, while the corresponding Q1-Q3 and median values are given in table 3. It can be seen that RS AGN show slightly larger values of log(X/O) flux ratio, with a median value of 0.59, in comparison to both GV and BC AGN that have a similar distribution with median value of 0.24. In addition, the Q1-Q3 range of GV and BC AGN (-0.12 - 0.6), is slightly lower than the one of RS AGN (-0.04 - 0.8), as indicated in table 4.3.

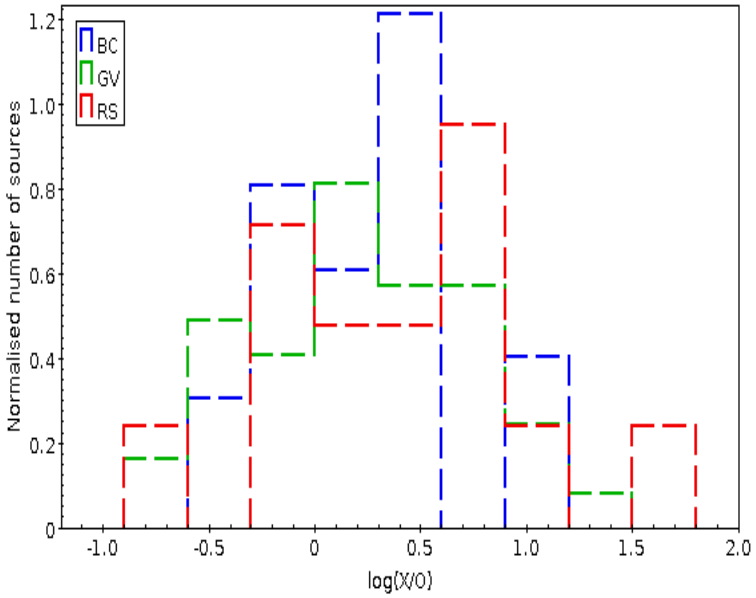

Figure 4.5: Normalised distribution of X-ray-to-optical flux ratio of BC, GV, and RS AGN, as indicated in the labels.

4.2.2 Hardness ratio distribution

The hardness ratio (HR), known as the X-ray colour, has been commonly used for AGN classification in X-rays, in particular, to separate between X-ray type-1 (or unobscured) and X-ray type-2 (or obscured) sources. We computed the HR as in Pović et al. (2009a,b), using the count rates (CR) in different available Chandra and XMM-*Newton* X-ray bands. In total, we computed three different HRs:

$$HR1\left(\frac{2-5keV}{0.5-2keV}\right)=\frac{CR(2-10keV)-CR(5-10keV)-CR(0.5-2keV)}{CR(2-10keV)-CR(5-10keV)+CR(0.5-2keV)} \tag{4.6}$$

$$HR2\left(\frac{2-10keV}{0.5-2keV}\right)=\frac{CR(2-10keV)-CR(0.5-2keV)}{CR(2-10keV)+CR(0.5-2keV)} \tag{4.7}$$

$$HR3\left(\frac{2-7keV}{0.5-2keV}\right)=\frac{CR(2-7keV)-CR(0.5-2keV)}{CR(2-7keV)+CR(0.5-2keV)} \tag{4.8}$$

We were able to measure HR1 for 10% of AGN in total, having X-ray fluxes available in all indicated X-ray bands. Out of these, 60, 64, and 26 are BC, GV, and RS AGN, respectively. HR2 was measured for a a total of 456 (32%) sources. Out this, we found 187 BC, 189 GV, and 80 RS AGN. Finally, HR3 was measured for a total of 1250 (88%) AGN, out of which we have 430 (29%) BC, 550 (38%) GV, and 270 (18%) RS AGN.

Figure 4.6 shows the distribution of HR1 (top left), HR2 (top right), and HR3 (bottom) of BC (blue dashed line), GV (green dashed line), and RS (red dashed line) AGN. In all cases, independently on the X-ray bands, BC AGN shows lower values of HR in comparison to GV and RS AGN whose values are very similar in terms of both median and Q1-Q3 ranges. Tables 4.2 and 4.3 can be consulted for all measured median and Q1-Q3 values. This suggests that, in general, BC AGN are more unobscured in comparison to GV and RS AGN (see the next section for more info).

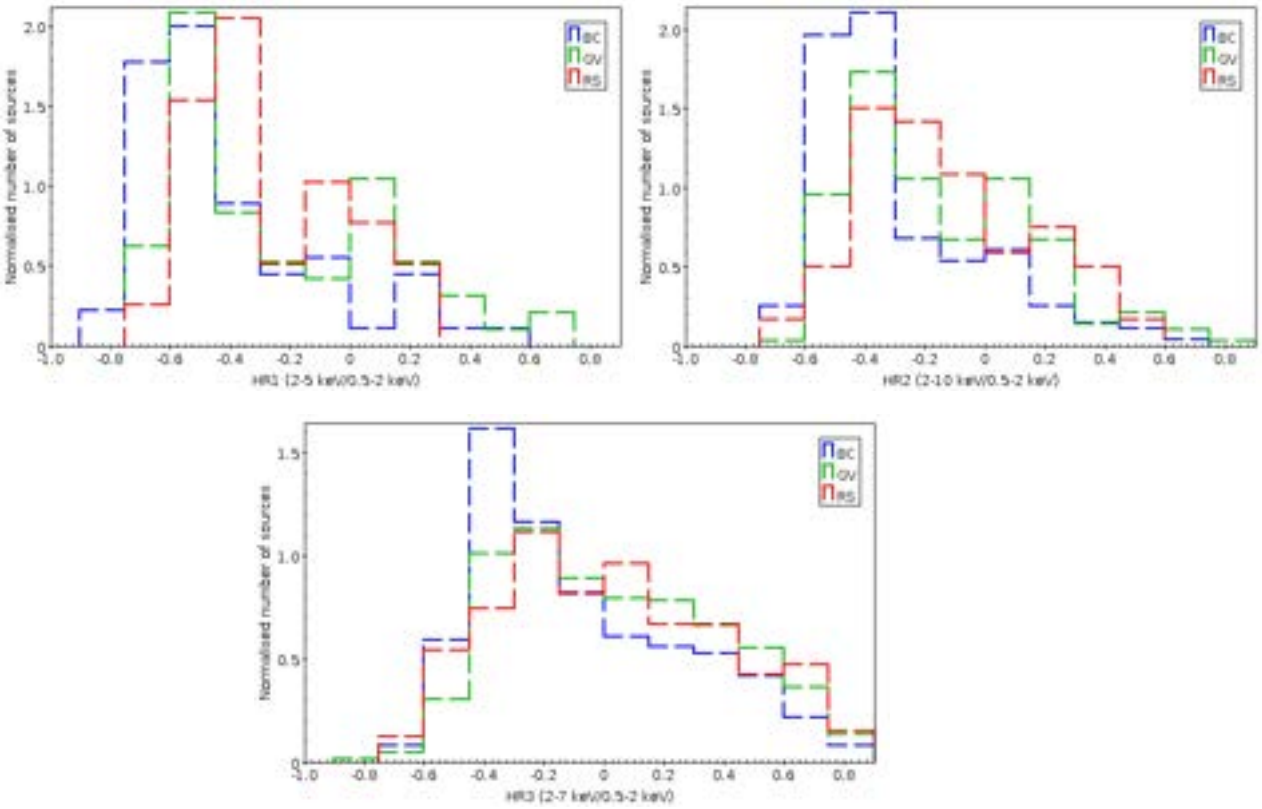

Figure 4.6: Normalised distribution of HR1 (top left), HR2 (top right) and HR3 (bottom) of BC, GV, and RS AGN, as indicated in the labels.

4.2.3 The HR versus X/O distribution

We applied a simple criterion in a nuclear-type classification of our AGN sample, based on a diagnostic diagram that connects the X-ray-to-optical ratio and HR. This criterion was used in previous works, and in particular we followed the results of Pović et al. (2009a,b), based on the results of Della Ceca et al. (2004) using the spectroscopic data of the XMM-*Newton* Bright Serendipitous Survey. In those works, HR(2 - 4.5keV/0.5 - 2keV) was used and the X/O ratio using the 0.5-4.5ke X-ray band and optical R filter. We used in optical R band as well for measuring the X/O flux ratio, as indicated above, and 2 - 5keV XMM-*Newton* hard X-ray band since being the closest one to the 2 - 4.5keV band. The relation between the X/O flux ratio and HR1 is shown in figure 4.7 for BC (blue diamonds), GV (green crosses), and RS (red open squares) AGN. In total, the data are available for 87 (7%) sources, out of which 32, 41, and 14, are BC, GV, and RS AGN, respectively. To select whether the galaxies are type-1 or type-2, we used the following conditions: log (X/O) > -1 and HR < - 0.35 for unobscured,

and log (X/O) > -1 and HR > - 0.35 for obscured AGN, respectively (Della Ceca et al. (2004); Pović et al. (2009a, b)). We found that 69% (31%), 37% (63%), and 21% (79%) of BC, GV, and RS AGN are unobscured (obscured) sources, respectively. BC is more unobscured than GV and RS.

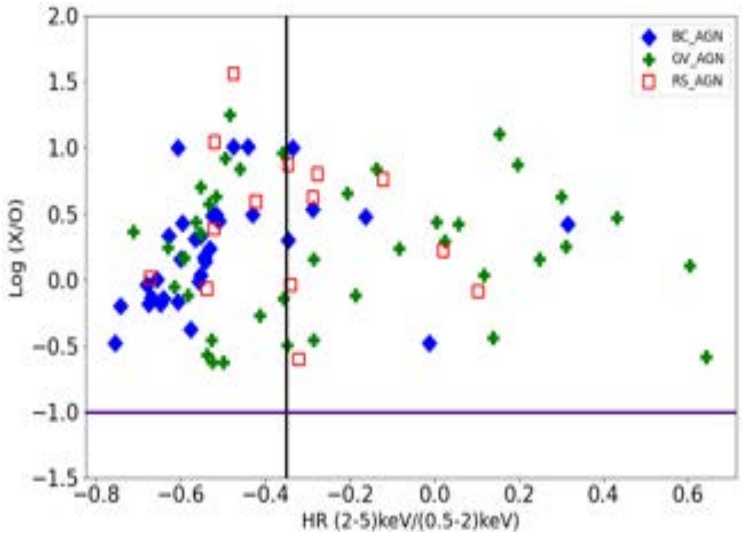

Figure 4.7: Relation between the X/O flux ratio and HR1 as defined in eq 4.6 of BC, GV, and RS AGN, as indicated in the labels. Horizontal and vertical solid lines mark the border for unobscured AGN (above the horizontal line and left of the vertical line) and obscured AGN (above the horizontal line and right of the vertical line).

4.2.4 The luminosity distribution

Using the K-corrected fluxes as defined in section 4.2.1, we measured the X-ray luminosity as:

$$L_X = 4\pi d_L^2 \times Fx_{,kcor}\,, \tag{4.9}$$

where d_L is the luminosity distance defined as: the relationship between bolometric (i.e, integrated over all frequencies) flux S and bolometric luminosity L (e.g., Hogg (1999)):

$$d_L = \sqrt{\frac{L}{4\pi s}}, \tag{4.10}$$

We measured the luminosity distance directly through the function that is implemented in TOPCAT, extracting the redshift information from the AGN catalogue (see section 4.1) and assuming the cosmological model of the flat universe with values of Hubble constant $\sim 70 H_0$, Ω_M = 0.3, Ω_Λ= 0.7.

The distributions of all four measured X-ray luminosities are shown in figure 4.8 for BC (blue dashed lines), GV (green dashed lines), and RS (red dashed lines) AGN. For each X-ray luminosity and BC, GV, and RS AGN samples, we measured the median and Q1-Q3 range, as can be seen in tables 4.2 and 4.3. In general, in all cases we obtain very similar distributions of BC, GV, and RS AGN, finding very similar values for both median and Q1-Q3 ranges occupied by 50% of sources.

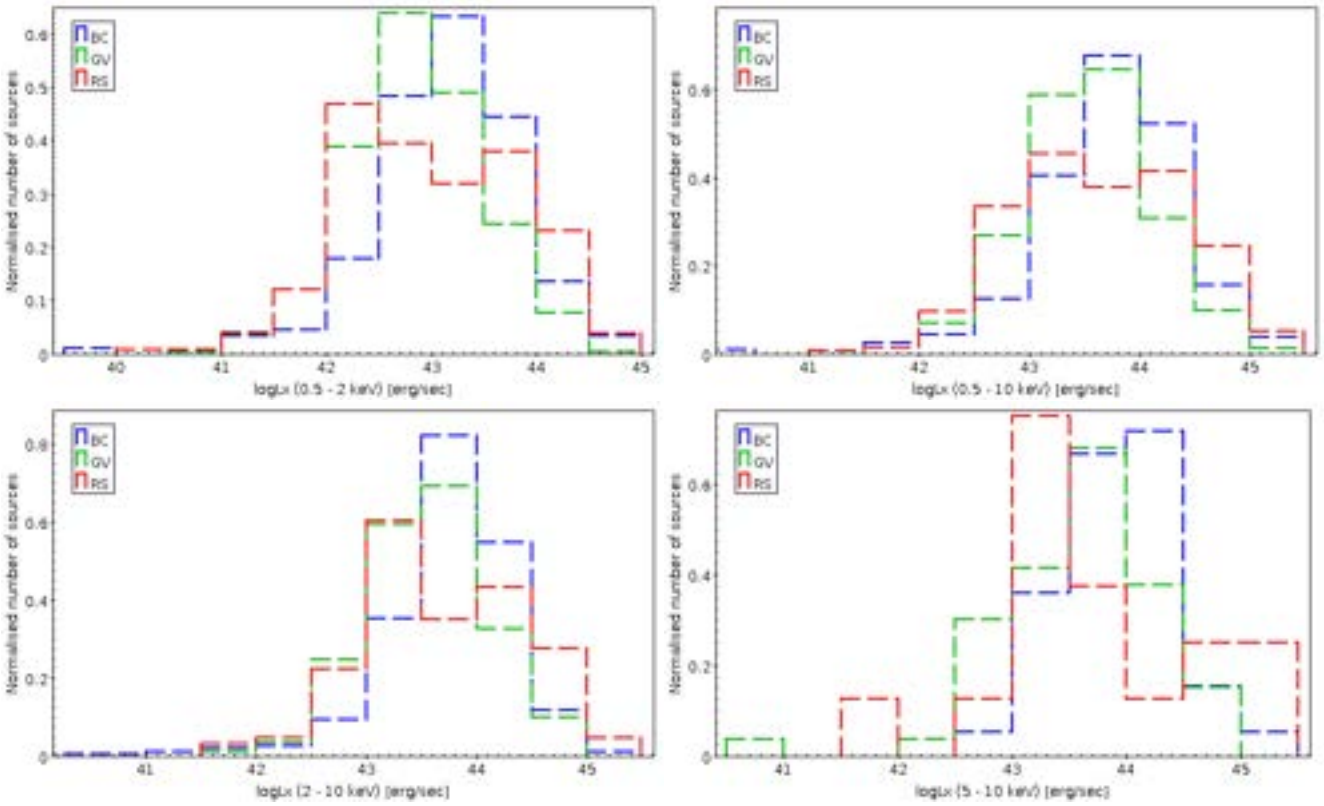

Figure 4.8: Normalised distribution of X-ray luminosity in the 0.5 - 2 keV (top left), 0.5 - 10 keV (top right), 2 - 10 keV (bottom left), and 5 - 10 keV (bottom right) bands of BC, GV, and RS AGN, as indicated in the labels.

4.2.5 X-ray luminosity versus redshift and stellar mass

In the previous section, we measured the logarithm of k-corrected X-ray luminosity in BC, GV, and RS for the different energy bands in Chandra (see equations 4.9). In addition, we have already extracted redshifts and stellar masses from Salvato et al. (2011) and Mahoro et al. (2017) catalogues, as described in sections 4.1.2 and 4.1.3, respectively. In this subsection, we compared the X-ray luminosity in the 2-10 keV band using the data of Chandra with the redshift and stellar mass. These relations are common ones used in X-ray studies for general check-ups. We wanted to test the location of our BC, GV, and RS AGN on these commonly-used diagrams. Figure 4.9 (left plot) shows the 2 - 10 keV luminosity-redshift plane of the BC (blue diamonds), GV (green crosses), and RS (red open squares) AGN. We can see that BC, GV, and RS AGN have a similar distribution in the X-ray luminosity-redshift plane, as expected since only Chandra data have been used here. Figure 4.9 (right plot) compares the distribution of all AGN observed in Chandra (red symbols) and XMM-*Newton* (green symbols) in the luminosity-redshift plane. It can be seen that XMM-*Newton* data are more shalow, as expected taking into account a much smaller number of sources (497 or 34%) in comparison to Chandra (1273 or 86%).

Finally, figure 4.10 shows the 2 - 10 keV X-ray luminosity of BC, GV, and RS AGN as a function of stellar mass. It can be seen that at fixed stellar mass, galaxies have systematically higher X-ray luminosities. This trend can be seen in the case of all BC, GV, and RS AGN, and the results are in line with previous studies (e.g., Mullaney et al.(2012), Georgakakis et al. (2017)). The goodness factors of the linear fits obtained for the three samples are 0.66, 0.44, and 0.57, for BC, GV, and RS AGN, respectively.

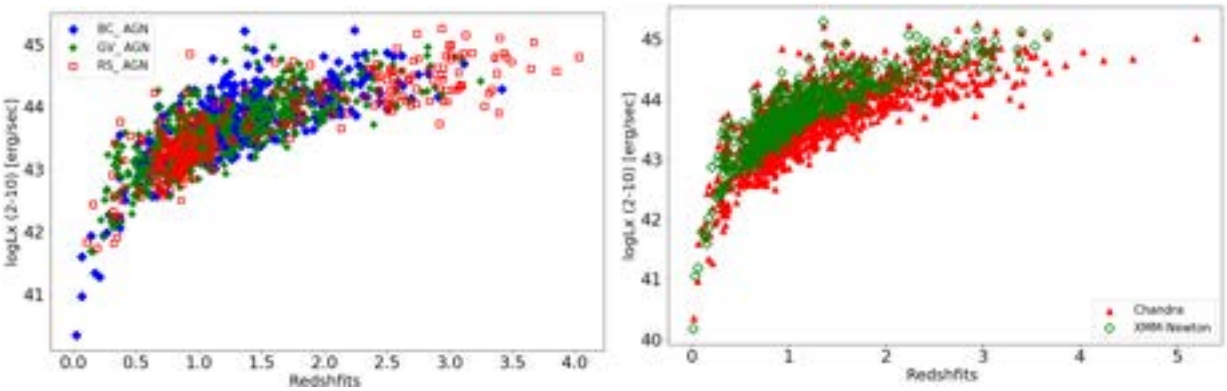

Figure 4.9: The 2 - 10 keV X-ray luminosity-redshift plane of the BC (blue diamonds), GV (green crosses), and RS (red open squares) AGN.

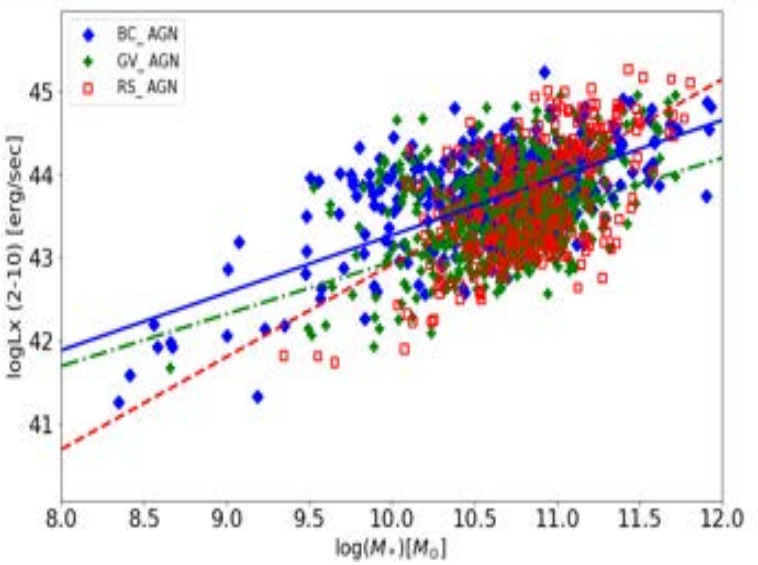

Figure 4.10: The linear correlation of X-ray luminosity of BC (blue diamonds), GV (green crosses), and RS (red open squares) AGN as a function of stellar mass.

4.3 Radio analysis

In this section, we focused on the analysis of radio properties of BC, GV, and RS AGN, using the information provided in Schinnerer et al. (2010), Smolčić et al. (2017), and Vardoulaki et al. (2021) radio catalogues described in chapter 3. We analysed several properties such as the radio luminosities at 1.4 and 3 GHz, X-ray to radio luminosity ratio, jet luminosity, and radio classification. In addition, we used the availability of additional parameters, such as the SFR and SMBH mass to test their distributions for our sample of BC, GV, and RS galaxies. Finally, we also checked the location of all of our AGNs on the SFR-stellar mass plane. For all analysed parameters, we measured the median values and Q1 - Q3 range, as in previous sections, as can be seen in table 4.4.

Table 4.4: Statistical summary of analysed parameters in radio.

BC AGN			
No	Analysed parameter	Q1 – Q3	Median
1	L_{radio} at 1.4 GHz	23.25 – 23.90	23.54
2	L_{radio} at 3 GHz	23.02 – 23.64	23.34
3	Lx/L_{radio}	3.14 – 4.13	3.72
4	λr	-2.09 – -0.94	-1.47
5	λrk	-1.60 – -0.80	-1.29
6	logLjet	43.72 – 44.22	43.99
7	$\log_{MBH}$	8.01 – 8.35	8.18
8	log(SFR)	1.20 – 1.91	1.57

GV AGN			
No	Analysed parameter	Q1 – Q3	Median
1	L_{radio} at 1.4 GHz	23.03 – 23.93	23.40
2	L_{radio} at 3 GHz	22.78 – 23.68	23.16
3	Lx/L_{radio}	3.08 – 3.85	3.48
4	λr	-2.52 – -1.65	-2.07
5	λrk	-2.29 – -1.39	-1.79
6	logLjet	43.54 – 44.18	43.93
7	$\log_{MBH}$	8.14 – 8.59	8.36
8	log(SFR)	0.90 – 1.77	1.36

RS AGN			
No	Analysed parameter	Q1 – Q3	Median
1	L_{radio} at 1.4 GHz	23.07 – 24.15	23.48
2	L_{radio} at 3 GHz	22.86 – 23.97	23.25
3	Lx/L_{radio}	2.83 – 4.17	3.38
4	λr	-2.67 – -1.44	-2.36
5	λrk	-2.40 – -1.39	-2.09
6	logLjet	43.54 – 44.16	43.95
7	$\log_{MBH}$	8.23 – 8.61	8.43
8	log(SFR)	0.89 – 1.90	1.25

4.3.1 Radio luminosity at 1.4 GHz

We analysed the distribution of radio luminosity at 1.4GHz of BC, GV, and RS AGN. This luminosity corresponds to the emission at 21 cm of the cold neutral hydrogen (HI), and therefore it is important for understanding the properties of the interstellar medium and the dust-unbiased star formation properties of galaxies (i.e., log SFR = log L1.4 GHz + const., e.g., Condon (1992)). The luminosity values have been extracted directly from Schinnerer et al. (2010) described above in chapter, in the SI unit of log W/Hz. In total, 535 (36%) of our all AGN have 1.4GHz radio luminosity measured, out of which 162 (11%), 247 (17%), and 112 (8%) are BC, GV, and RS AGN, respectively, with 14 sources being out of the BC, GV, and RS limits. Figure 4.11 represents the radio luminosity at 1.4GHz distribution for the BC, GV, and RS AGN. As in all previous cases, we measured the median value for each AGN type and Q1-Q3 region. As can be seen from both figure 4.11 and table 4.4, we do not find significant differences between BC, GV, and, RS AGN. They all have a similar median value of 23.4 - 23.6 W/Hz, and also a similar Q1-Q3 range, as can be seen in table 4.4.

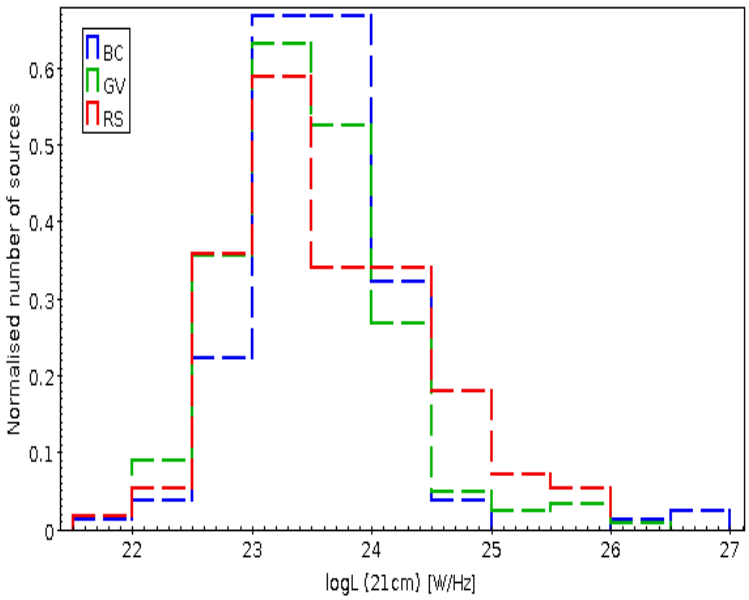

Figure 4.11: The distribution of radio luminosity at 1.4 GHz (21 cm) of BC, GV, and RS AGN, as indicated in the labels.

4.3.2 Radio luminosity at 3 GHz

Similar to the radio luminosity at 1.4 GHz, in this section, we analysed the distribution of radio luminosity at 3GHz (corresponding to a 10cm line). The emission at 3 GHz is important for galaxy classification, in particular for separating between the star-forming and AGN galaxies. We extracted the measured values from Smolčić et al. (2017) catalogue, as mentioned above in chapter 3. Extracted luminosity is again in SI units of log W/Hz. We extracted 3GHz luminosities for 535 (36%) AGN in total, out of which 162 (11%), 247 (17%), and 112 (8%) are BC, GV, and RS AGN, respectively. Figure 4.12 represents the distribution of 3GHz radio luminosity of BC, GV, and RS AGN. We compared the measured statistics for these galaxies. Similar as in the previous section, we do not find significant differences between BC, GV, and, RS AGN. They all have a very similar median value between 23.2 - 23.35 W/Hz, and similar Q1-Q3 range, as can be seen in table 4.4.

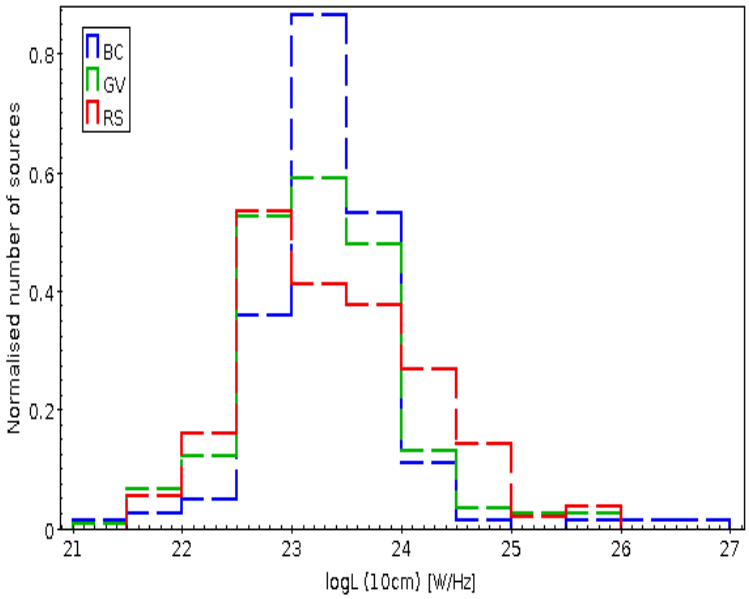

Figure 4.12: The distribution of radio luminosity at 3 GHz (10 cm) of BC, GV, and RS AGN, as indicated in the labels.

4.3.3 X-ray to radio luminositiy ratio

The Lx/L_{radio} ratio has already been meassured by Vardoulaki et al. (2021), as the ratio between the X-ray luminosity in 2 - 10 keV and radio liminosity at 1.4 GHz. The ratio has been extracted from the catalogue for a total of 134 sources, out of which 32, 68, and 34 are BC, GV, and RS AGN, respectively. A distribution of Lx/L_{radio} ratio of BC, GV, and RS AGN

is given in figure 4.13. It can be seen that, in general, Lx/L_{radio} ratio is slightly decreasing as going from BC to RS galaxies. The median values of Lx/L_{radio} ratio of BC, GV, and RS AGN are 3.72, 3.48, and 3.38, respectively, while 50% of AGN ocupy the range of 3.14 - 4.13, 3.08 - 3.85, 2.83 - 4.17, respectively.

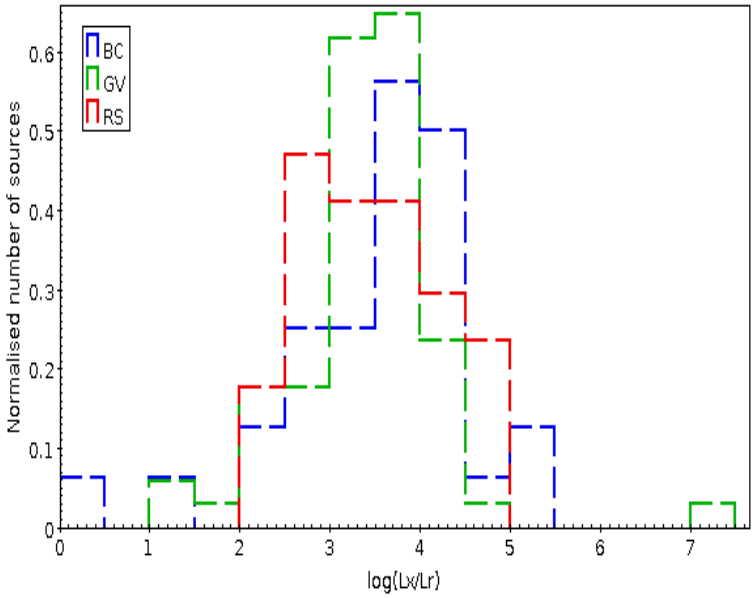

Figure 4.13: The distribution of Lx/L_{radio} of BC, GV, and RS AGN as indicated in the labels.

4.3.4 Classification using radio catalogues

We used the classification of sources available in Smolčić et al. (2017) catalogue. Using the ratio between the 1.4 GHz radio luminosity and SFR measured in IR, the authors classified the radio detected sources into:

1. moderate-to-high radiative luminosity AGN (HLAGN, referring to X-ray-, MIR-, and SED-selected AGN, regardless of their radio excess in
log (L1.4 GHz /SFR_{IR}), and

2. low-to-moderate radiative luminosity AGN (MLAGN, referring to the AGN identified-via quiescent, red host galaxies, or those with a $> 3\sigma$ radio excess in log (L1.4 GHz /SFR_{IR}), but not identified as X-ray, MIR, or SED AGN.

In total, the authors provided several classifications such as if the source is: X-ray AGN, mid-IR AGN, SED AGN, quiescent MLAGN, star-forming galaxy, no radio-excess SFG, HLAGN, MLAGN, and with radio-excess. Brifly, the following criteria were used in the selection:

- X-ray AGN, mid-IR AGN, and/or SED AGN, if the source shows AGN signatures in X-rays, MIR, and through SED fitting, respectively (for more information see Smolčić et al. (2017)).
- HLAGN were selected with a combination of 2-10 keV X-ray luminosity (Lx > 10^{42} erg/s), MIR color–color Donley et al. (2012), and SED-fitting Delvecchio et al. (2017) criteria.
- Star-forming galaxies (SFGs), if it is not HLAGN, and if it has the dust-extinction corrected rest-frame color i) M_{NUV} - Mr+ < 3.5, or ii) M_{NUV} - Mr+ > 3.5 but with available Herschel detections.
- MLAGN were drawn from the sample remaining after exclusion of the HLAGN.

  They have been further classified into:

  - Quiescent MLAGN, if M_{NUV} - Mr+ > 3.5 and there is no detection in any of the Herschel bands (at $\geq 5\sigma$ level).
  - Radio excess MLAGN, if objects have a $> 3\sigma$ radio excess in the redshift-dependent distribution of log(L1.4 GHz/SFR_{IR}).

Out of all AGN, we have the classification available for 162, 247, and 112 BC, GV, and RS AGN, respectively. Table 4.5 gives the details regarding the final classification of BC (top), GV (middle), and RS (bottom) AGN, taking into acount the above classes and either “True” or “False” flags. It can be seen that all BC, GV, and RS AGN are principally classified as HLAGN, with a very small number of sources being MLAGN. As expected, a significant number of sources with AGN signatures is classified as ’True’ in X-rays, MIR, and through SED fitting, and very small fraction of SFGs or Clean SFGs has been classified as ’True’ in the case of all BC, GV, and RS AGN.

Table 4.5: Classification for BC, GV, and RS from Smolčić et al. (2017) studies.

BC AGN			
No	Analysed parameter	No of true values	No of false values
1	X-ray-AGN	133	29
2	MIR-AGN	54	108
3	SED-AGN	97	65
4	QMLAGN	3	159
5	SFG	15	147
6	Clean SFG	14	148
7	HLAGN	141	21
8	MLAGN	4	158
9	RExcess	36	126

GV AGN			
No	Analysed parameter	No of true values	No of false values
1	X-ray-AGN	226	21
2	MIR-AGN	47	200
3	SED-AGN	107	140
4	QMLAGN	2	245
5	SFG	13	234
6	Clean SFG	10	237
7	HLAGN	231	16
8	MLAGN	5	242
9	RExcess	71	176

RS AGN			
No	Analysed parameter	No of true values	No of false values
1	X-ray-AGN	95	17
2	MIR-AGN	27	85
3	SED-AGN	52	60
4	QMLAGN	7	105
5	SFG	4	108
6	Clean SFG	3	109
7	HLAGN	100	12
8	MLAGN	8	104
9	RExcess	42	70

FR-classification

The Fanaroff-Riley (FR) classification is a scheme based on extended radio morphologies (e.g., presence of jets and lobes) of radio galaxies (Fanaroff and Riley, (1974)). In this work, we extracted the FR classification from Vardoulaki et al. (2021). Although this classification is available only for 13 sources, we present here the results. The authors measured the.structure and classified sources as FR1, FRII, hybrid, and radio sources based on the following criteria:

- FRI or edge-darkened, if the distance from the centre to the brightest point along their structure is less than half of the total size of the source, and if they show jets.
- FRII or edge-brightened, if the distance from the centre to the brightest point along their structure is more than half of the total size of the source, and if it displays lobes.
- FRI/FRII is also called a hybrid, as one side is FRI and the other is FRII.
- Radio source (RS): has neither of above characteristics.

Finally, we found all the sources in BC, two in total, are classified as FRII. Out of seven GV AGN, two are classified as FRI/FRII, three as FRII, and two as FRI, whereas, out of four RS AGN, one is classified as FRI and three as FRII radio sources. However, the statistics available are too small for raising any conclusions.

4.3.5 The λr, λrk, and jet luminositiy

A black hole's ability to absorb matter from its surroundings is directly correlated with a physical quantity called the Eddington ratio. It describes the ratio of the luminosity emitted by the source to the Eddington luminosity, which is the highest luminosity an object may reach when its gravitational pull and radiation emission are equal (e.g., Heckman and Best (2014); Netzer et al. (2015), and references therein).
In this work, we used the Eddington ratios measued in Vardoulaki et al. (2021). They have been measured in two ways:
λr can be meassured using the following mathematical formula:

$$\lambda r = \frac{Lrad}{LEdd}, \tag{4.11}$$

where Lrad is radiative luminosity and LEdd is Eddington luminosity.
λrk can be meassured using the following mathematical formula:

$$\lambda rk = \frac{Lrad + Q_{jet}}{LEdd}, \tag{4.12}$$

where Lrad and LEdd are as in eq. (4.12), with the addition of the jet kinetic energy to the numerator. Kinetic energy was was calculated from the radio luminosity at 1.4 GHz using

the empirical relation by Cavagnolo et al. (2010), and was extracted from Vardoulaki et al. (2021) catalogue. To measure Lrad, scaled to bolometric luminosities, the authors used a set of luminosity-dependent bolometric corrections from Lusso et al. (2012). The Eddington luminosity was calculated using the conversion MBH = Mbulge ~ 0.002 from Marconi & Hunt (2003), where Mbulge is assumed to be M* estimated from the SED fitting (Delvecchio et al. (2017)).

Figure 4.14 hows the distribution of λr (top left), λrk (top right), and jet luminosity (bottom) of BC, GV, and RS AGN, while the median and Q1-Q3 ranges for each distribution are listed in table 4.4. It can be seen from both figures and the table that BC AGN show in average higher values of Eddington ratio, measured through both λr and λrk, in comparison with GV and RS AGN, where GV show again higher values in comparison with RS AGN. These results go in line with Pović et al. (2009a, 2009b), where it was suggested that LT galaxies are accreting on higher rates, perhaps due to the larger amount of gas and dust available. Regarding jet luminosity, we do not find any significant differences between the three samples of AGN. A larger sample is needed for further analysis.

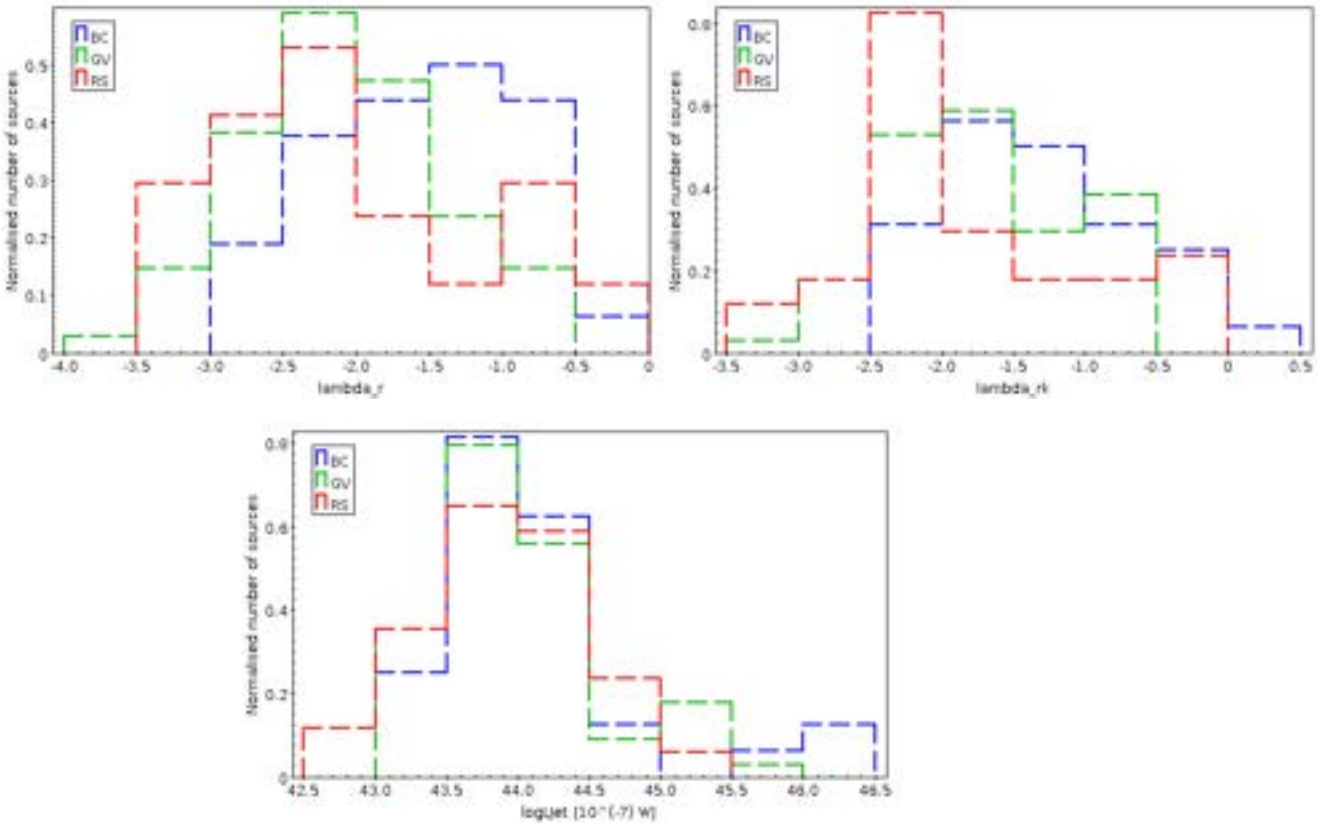

Figure 4.14: Normalised distribution of λr (top left), λrk (top right), and jet luminosity (bottom) of BC, GV, and RS AGN, as indicated in the labels of each plot.

4.4 Black hole mass and SFR properties

In this section, we analysed the black hole mass and SFR distributions of a sub-sample of our AGN, and the SFR-M* plane.

4.4.1 The black hole mass (MBH)

Black hole masses are essential for understanding the physics of accretion and emission processes in the BH environment and the relationship between BH growth and galaxy stellar population evolution. Black hole mass was previously measured using H_β emission-line widths and luminosities and was extracted for this work from Vardoulaki et al. 2021 catalogue mentioned above in chapter 3. The BH mass was measured using the relation of, Juna et al. (2006):

$$\log M_{BH} = a + b \log(\lambda L_{44}) + 2 \log V, \tag{4.13}$$

where M_{BH} is the estimated black hole mass in units of $M_{\odot}$, V is the H_{β} with full width at half-maximum in km s^{-1}, and $L\lambda L_{44}$ is the continuum luminosity near the line. Out of all AGN in our sample, 134 sources have MBH available, out of which 32, 68, and 34 are BC, GV, and RS AGN, respectively. Figure 4.15 shows the BH mass distribution of our sample of BC, GV, and RS AGN. In this subsection, we compared the BC, GV, and RS, of their statistical analysis. From both figure 4.15 and table 4.4, it can be seen that the BH mass is decreasing as going from the RS, through GV, to BC AGN. RS AGN has the highest BH mass with a median logMBH of $8.43M_{\odot}$ and 50% of sources being in the range of 8.23 - $8.61M_{\odot}$. GV AGN have median logMBH of $8.36M_{\odot}$ and Q1 - Q3 range of 8.14 - $8.59M_{\odot}$. Finally, BC AGN has a median logMBH of $8.18M_{\odot}$ and Q1 - Q3 range of 8.01 - $8.35M_{\odot}$. These results are in line with the previous, showing that in general RS sources, with a larger fraction of ET galaxies, have the largest BH masses (e.g., see Urry and Woo (2002), Best and Heckmann et al. (2014), for reviews and references therein).

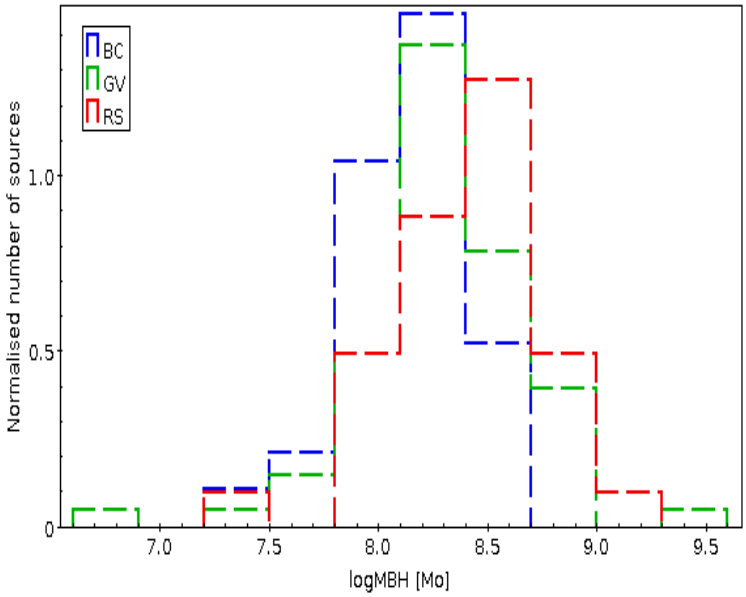

Figure 4.15: The normalised blackhole mass distribution of BC, GV, and RS AGN as, indicated in the labels.

4.4.2 The SFR

The SFR is one of the most fundamental parameters for studying the evolution of galaxies, showing the number of stars of solar mass formed per year, as indicated above, and can be expressed as M⊙/yr. In this work, we used the SFR information available in the Smolčić et al. (2017) catalogue, derived from the total IR emission in the host galaxies as computed via the

three-component SED fitting procedure (Delvecchio et al. (2017)). Therefore, as indicated in Smolčić et al. (2017), SFRs were obtained from SED fitting using the total (8 - 1000 μm rest-frame) infrared luminosity obtained from the best-fit galaxy template for sources both with and without Herschel detection (Delvecchio et al. (2017)). Authors indicated that this luminosity represents the fraction of the total IR luminosity arising from star formation for X-ray-, MIR-, and SED-selected AGN, or the total IR luminosity otherwise, and that it was converted to SFR via the Kennicutt (1998) conversion factor and scaled to a Chabrier (2003) initial mass function (IMF). Out of all AGN in our sample, 481 sources have SFR available, out of which 151 (10%), 225 (15%), and 105 (7%) are BC, GV, and RS AGN, respectively. Figure 4.16 shows the distribution of SFR for BC, GV, and RS AGN, while the measured statistics are available in table 4.4. It can be seen from both figure 4.16 and table 4.4, that BC AGN show higher values of SFR, having median log (SFR) of 1.57 $M_{\odot}$/yr in comparison to GV and RS median values of 1.36 and 1.25 $M_{\odot}$/yr, respectively. The Q1 - Q3 range of BC AGN is also taking larger values, with 50% of sources having log (SFR) in the range of 1.20 - 1.91 $M_{\odot}$/yr, in comparison to 0.9 - 1.77 $M_{\odot}$/yr, and 0.89 - 1.90 $M_{\odot}$/yr. This is again in line with previous results, expecting to have more LT galaxies in the BC, with higher SFRs.

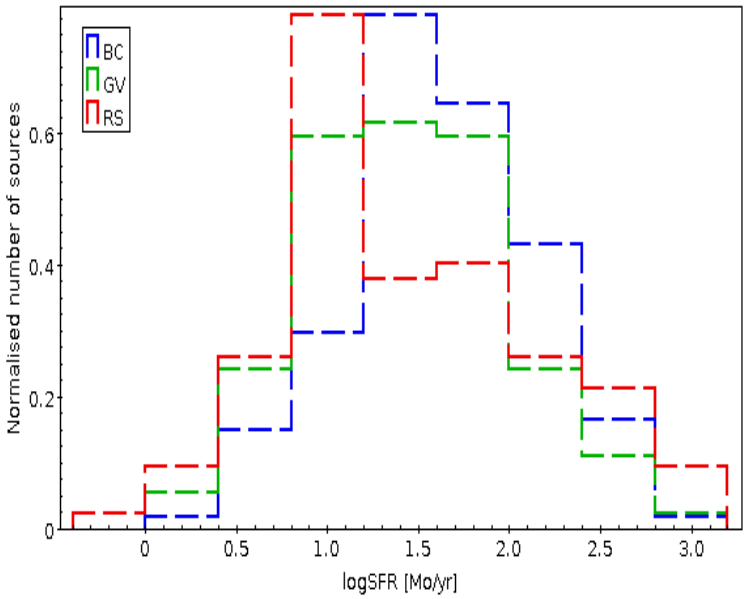

Figure 4.16: The normalised SFR distribution of BC, GV, and RS AGN as indicated in the labels.

4.4.3 The relation between the SFR and stellar mass

In this section, we analyse the location of our AGN sample on the SFR vs. stellar mass diagram and the main sequence of star formation. Figure 4.17 shows the mentioned diagram.

For SFR we used the IR measurements extracted from Smolčić et al. (2017), as explained in section 4.3.1. Stellar masses have been extracted from the catalogue of Mahoro et al. (2017), as explained above in section 4.1.3. To plot the main sequence of star formation, as a reference we used the results of Elbaz et al. (2011), obtained also through IR SFR measurements. In figure 4.17, the main sequence is represented using the solid line, while the typical width of the main sequence of $\pm$ 3dex is shown with dashed lines. We presented the location of our BC (blue diamonds), GV (green crosses), and RS (red open squares) AGN and the main sequence of star formation. A very similar distribution of sources can be observed in case of all BC, GV, and RS AGN. We can see that in all three cases, there are sources located on, above, and below the MS of SF. This is fully in line with Mahoro et al. (2017 and 2019) for GV AGN, as expected since we are using the same sample and IR measurements of SFRs. However, in this work we can see that BC and RS MIR AGN show very similar properties as well. In the future, SFRs used in this work shall be compared with the SFRs of Mahoro et al. (2017) for GV AGN, where a special care has been taken into account for measuring the SFRs of AGN. A special care shall then be placed on BC and RS SFRs measurements, for confirming the above findings.

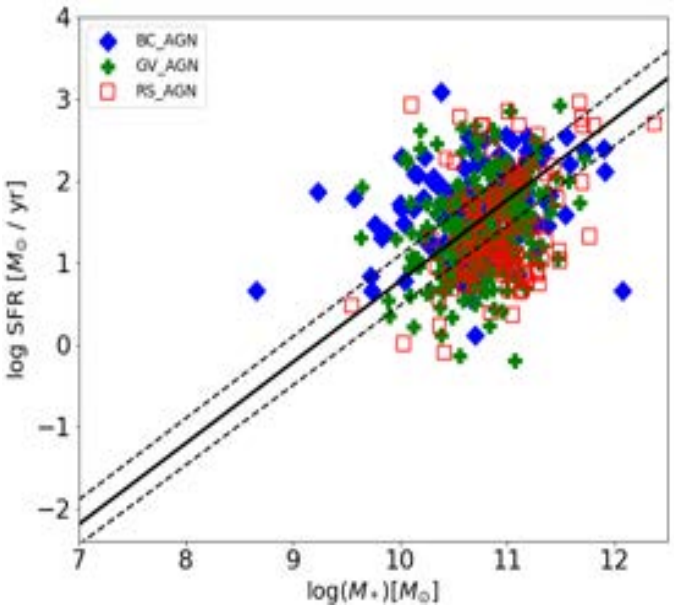

Figure 4.17: Relation between the SFR and stellar mass of BC (blue diamonds), GV (green crosses), and RS (red open squares) AGN.

Chapter 5

Discussion and conclusions

In this work, we analysed a sample of 1472 X-ray detected AGN in the COSMOS field. We performed a multiwavelength study by analysing a number of parameters in optical, X-rays, and radio of the BC, GV, and RS AGN selected through the commonly used U-B rest-frame colour criteria. This work was inspired by the results of Mahoro et al. (2017), who found that, within the same stellar mass range, GV selected FIR AGN show enhanced SFRs in comparison to non-AGN sources. We wanted to go a step further and understand what kind of AGN these sources are, focusing in particular on their X-ray and radio properties. We, however, extended our studies to all regions, BC, GV, and RS, for obtaining the more broad picture. In optical, we had a look at the basic distributions of BC, GV, and RS AGN in terms of their redshift, stellar mass, and absolute magnitudes in B and F814W bands. In X-rays, we analysed several properties using different X-ray bands, such as the X-ray-to-optical flux ratio, X-ray colours or hardness ratios, and X-ray luminosities. In addition, we analysed the location of sources on the X/O-hardness ratio plane, on the X-ray luminosity-redshift plane, and on the X-ray luminosity-stellar mass plane. In radio, we analysed several properties such as the radio luminosities at 1.4 GHz and 3 GHz, X-ray to radio luminosity ratio, 2 types of accretion rates, jet luminosity, and radio classification. Finally, we used the availability of additional parameters, such as the SFR and SMBH mass to test their distributions for our sample of BC, GV, and RS AGN, and to check the location of all AGN on the SFR-stellar mass plane. In the following, we summarise and discuss our main findings.

* The highest fraction of X-ray detected AGN in the COSMOS field is located in the GV (41%), followed by the BC (35%), and finally RS (20%). This goes in line with previous AGN studies that found the largest fraction of X-ray detected AGN in the GV, considering samples at different redshifts (e.g., Nandra et al. (2007); Georgakakis et al. (2008); Silverman et al. 2008; Treister et al. (2009); Hickox et al. (2009); Cardamone et al. (2010); Pović et al. (2012)), and suggesting that AGN might be responsible for quenching the SF in galaxies.

* BC AGN, on average, show slightly lower stellar mass, with a median value of logM* = 10.59 $M_{\odot}$, in comparison to median stellar masses of GV and RS AGN of logM* = 10.73 $M_{\odot}$ and 10.86 $M_{\odot}$, respectively. Similarly, 50% of BC, GV, and RS AGN occupy the stellar mass range of logM* = 10.01 - 10.87 $M_{\odot}$ 10.45 - 10.95 $M_{\odot}$, and 10.60 - 11.13 $M_{\odot}$, respectively. Also, RS AGN are slightly brighter. All this goes in line with previous studies, considering the properties of BC, GV, and RS galaxies in general (e.g., Povi ć et al. (2013), Schawinski et al. (2014)). Here we can see that BC, GV, and RS active galaxies follow the same trend as non-active ones.

* RS AGN show slightly larger values of log(X/O) flux ratio, with a median value of 0.59, in comparison to both GV and BC AGN which have a similar distribution with a median value of 0.24. In addition, the Q1-Q3 range of GV and BC AGN ($\sim$ -0.12 - 0.6), is slightly lower than the one of RS AGN (-0.04 - 0.8). X/O flux ratio was not measured however for the majority of sources, and therefore this could change if a larger sample of sources is available. On the other side, independently of the X-ray bands used, BC AGN show lower values of HR in comparison to GV and RS AGN whose values are very similar in terms of both median and Q1-Q3 ranges. We found that 69% (31%), 37% (63%), and 21% (79%) of BC, GV, and RS AGN are unobscured (obscured) X-ray sources, respectively, when using the X/O vs. HR1(2-5keV/0.5-2keV) hardness ratio. In general, in all cases we obtained very similar distributions of X-ray luminosities in all 4 analysed X-ray bands between BC, GV, and RS AGN. We also found that BC, GV, and RS AGN have a similar distribution in the 2-10keV X-ray luminosity-redshift plane. Finally, at fixed stellar mass, galaxies have systematically higher X-ray luminosities. This trend can be seen in the case of all BC, GV, and RS AGN, and the results are in line with previous studies (e.g., Mullaney et al. (2012), Georgakakis et al. (2017)).

* We analysed the distribution of radio luminosities at 1.4GHz (at 21cm) and 3GHz (at 10cm) of BC, GV, and RS AGN. In both cases, we do not find significant differences between BC, GV, and, RS AGN. They all have a similar median value of 23.4 - 23.6 W/Hz in the case of 1.4GHz luminosity, and 23.2 - 23.35 W/Hz in the case of 3GHz luminosity and also similar Q1-Q3 ranges. On the other side, a small difference between BC, GV, and RS AGN has been observed when analysing the Lx/Lradio ratio, which is decreasing as going from BC to RS galaxies. The median values of Lx/Lradio ratio of BC, GV, and RS AGN are 3.72, 3.48, and 3.38, respectively, while 50% of AGN occupy the range of 3.14 - 4.13, 3.08 - 3.85, and 2.83 - 4.17, respectively. The great majority of BC, GV, and RS AGN are classified as moderate-to-high radiative luminosity AGN or HLAGN, and only a small fraction of sources as low-to-moderate radiative luminosity AGN or MLAGN.

* We used the Eddington ratios measured in Vardoulaki et al. (2021) in two different ways, as described in section 4.3.5. BC AGN show higher values of Eddington ratio in

comparison to GV and RS AGN, with GV showing higher values in comparison to RS AGN. These results go in line with Pović et al. (2009a), (2009b), where it was suggested that late-type galaxies are accreting at higher rates, perhaps due to the larger amount of gas and dust available.

* We compared the black hole masses of BC, GV, and RS AGN, and found that the BH mass is decreasing as going from RS, through GV, to BC AGN. RS AGN have the highest BH mass with a median logMBH of 8.43$M_{\odot}$ and 50% of sources being in the range of 8.23 - 8.61$M_{\odot}$. GV AGN have a median logMBH of 8.36$M_{\odot}$ and Q1 - Q3 range of 8.14 - 8.59$M_{\odot}$. Finally, BC AGN have a median logMBH of 8.18$M_{\odot}$ and Q1 - Q3 range of 8.01 - 8.35$M_{\odot}$. These results are in line with the previous, showing that in general RS sources, with a larger fraction of early-type galaxies have the largest BH masses (e.g., Urry and Woo (2002); Best and Heckmann et al. (2014); Netzer (2015), and references therein).

* We used the SFR information available in the Smolčić et al. (2017) catalogue, derived from the total IR emission in the host galaxies as computed via the three-component SED fitting procedure (Delvecchio et al. (2017)). BC AGN show higher values of SFR, having a median log (SFR) of 1.57$M_{\odot}$/yr in comparison to GV and RS median values of 1.36 and 1.25 $M_{\odot}$/yr, respectively. The Q1 - Q3 range of BC AGN is also taking larger values, with 50% of sources having log (SFR) in the range of 1.20 - 1.91$M_{\odot}$/yr, in comparison to 0.9 - 1.77$M_{\odot}$/yr, and 0.89 - 1.90$M_{\odot}$/yr, respectively. This is again in line with previous results, expecting to have more late-type galaxies in the BC, with therefore higher SFRs.

* Finally, we analysed the location of our AGN sample on the SFR vs. stellar mass diagram and the main sequence of star formation, plotted using the results of Elbaz et al. (2011), obtained through the IR SFR measurements. We obtained a very similar distribution of sources in the case of all BC, GV, and RS AGN. We can see that in all three cases, there are sources located on, above, and below the MS of SF. This is fully in line with Mahoro et al. (2017 and 2019) for GV AGN, as expected since we are using the same sample and IR measurements of SFRs as in the case of two previous works. In this work, we can see that BC and RS MIR AGN show very similar properties to GV AGN.

To summarise, BC, GV, and RS active galaxies show in general very similar properties in X-rays and radio, and even when the differences are observed the range of covered parameters is rather narrow. We confirmed the results obtained by Mahoro et al. (2017, 2019, and 2022) and found that in addition to GV AGN, BC and RS FIR AGN also show enhanced SFRs , confirming more complex scenarios of the role of AGN in star formation quenching when using multiwavelength data and the need for further studies.

References

Adhikari, T. P., et al., 2018, ApJ, 856, 78

Agarwal, A., et al., 2019, MNRAS, 468, 4093

Alexander, D. M., et al., 2001, AJ, 122, 2156

Antonucci, R., et al., 1993, ARAA, 473, 31

Apashanka, D., et al., 2021, JCAP06, 045

Arnouts, S., & Ilbert, O., 2011, ASCL, ascl–1108

Barvainis, R., et al., 2005, ApJ, 618, 108

Bauer, F. E., et al., 2004, AJ, 128, 2048

Beifiori, A., et al., 2012, MNRAS, 419, 2497

Bellhouse, C., 2021, MNRAS, 500, 1285

Bennert, V., et al., 2021, ApJ, 921, 36

Bergh, V. S., 2009, ApJ, 702, 1502

Bhatta, J., & Duda G., et al., 2021, MNRAS, 508, 1446

Binney, J., & Scott, T., 2011, Princeton university press, 13

Blandford, R., & Meier, D., 2019, ARAA, 57, 467

Blanton, M. R., & Roweis, S., 2007, ApJ, 133, 734

Boizelle, B. D., et al., 2021, ApJ, 980,1

Bondi, M., et al., 2008, ApJ, 681, 1129

Boselli, A., et al., 2009, ApJ, 706, 1527

Brammer, G. B., et al., 2009, ApJ, 706, L173

Brescia, M., et al., 2019, MNRAS, 489, 663

Brinchmann, J., Richard, S., & Ellis, S., 2000, ApJ, 536, L77

Brusa, M., et al., 2007, ApJS, 172, 353

Brusa, M., et al., 2010, ApJ, 716, 348

Bruzual, G., & Charlot, S., 2003, MNRAS, 344, 1000

Bundy, K., Treu, T., & Ellis, R. S., 2007, ApJ, 665, L5

Caglar, T., et al., 2020, A&A, 634, A114

Cappelluti, N., et al., 2009, A&A, 497, 635

Cavagnolo, K. W., et al., 2010, ApJ, 720, 1066

Cazzoli, S., et al., 2018, MNRAS, 480, 1106

Chabrier, G., 2003, Astronomical Society of the Pacific, 115, 763

Chen, YC., & Yen-Chen, H., 2019, MNRAS, 485, 2492

Cid Fernandes, F., et al., 2011, MNRAS, 413, 1687

Civano, F., et al., 2012, ApJS, 201, 30

Civano, F., et al., 2016, ApJ, 819, 62

Coenda, V., Martınez, H. J., & Muriel, H., 2018, MNRAS, 473, 5617

Comastri, A., et al., 2011, A&A, 526, L9

Condon, J. J., et al., 1998, AJ, 115, 1693

Conselice, C., et al., 2014, MNRAS, 444, 1125

Contini, E., et al., 2019, ApJ, 882, 167

Cowie, L. L., & Songaila, A., 1977, Nature, 266, 501

Crossett, P. J., et al. 2014, MNRAS, 437, 2521

Davis, W., et al., 2019, ApJ, 880, 67

Davis, W., & Tchekhovskoy, A., 2020, ARAA, 58, 407

Delhaize, J., et al., 2017, A&A, 602, A4

Della Ceca, R., et al., 2004, A&A, 428, 383

Dey, B., et al., 2022, MNRAS, 515, 5285

Donley, J. L., et al., 2012, ApJ, 748, 142

Duncan, K., et al., 2014, MNRAS, 444, 2960

Dunlop, J., et al., 2003, MNRAS, 340, 1095

Eappen, R., et al., 2022, MNRAS, 516, 1081

Edge, A. C., et al., 1992, MNRAS, 258, 177

Elbaz, D., et al., 2011, A&A, 533, A119

Ellison, S., et al., 2016, MNRAS, 458, L34

Fanaroff, L., & Riley, M., 1974, MNRAS, 167, 31P

Fang, J. J., et al., 2013, A&A, 521, A27

Finoguenov, A., et al., 2007, ApJS, 172, 182

Fiore, F., et al., 2003, A&A, 409, 79

Falomo, R., et al., 2003, MNRAS, 343, 505

Freitas-Lemes, P. et al., 2017, MNRAS, 468, 3159

Frosst, M., et al. 2022, MNRAS, 514, 3886

Fuchs, J., 2014, A&A, 571, A72

Fukazawa, Y., et al., 2022, ApJ, 931, 138

Fukugita, M., 1995, Astronomical Society of the Pacific, 107, 945

Garofalo, D., 2022, PASP, 134, 1036

Gaspari, M., et al., 2019, ApJ, 884, 169

Gaur, H., et al., 2019, A&A 631, A46

Georgakakis, A., et al., 2017, MNRAS, 471, 2001

Gillman, S., et al., 2020, MNRAS, 492, 1492

Giommi, P., et al., 2012, MNRAS, 420, 2899

Greener, M. J., et al., 2022, MNRAS, 516, 1275

Gregg, B., Calzetti, D., & Heyer, M., 2022, ApJ, 928, 120G

Gunn, J. E., & Gott, J. R., 1972, ApJ, 176, 1

Hao, H., et al., 2014, MNRAS, 1090, 12

Hasinger, G., et al., 2007, ApJS, 172, 29

Heckman, T., & Best, P., 2014, ARA&A,52, 589

Helfand, D. J., et al., 2015, ApJ, 801, 26

Henghes, B. et al., 2022, MNRAS, 512, 1696

Hermosa Muñoz, et al., 2020, A&A, 634, A10

Hogg, D. W., et al., 1999, Princeton NJ, 08540

Ho, L. C., 2008, ApJS, 26, 104

Hopkins, A. M., et al., 2003, ApJ, 599, 971

Hughes, D. W., et al., 2006, JAHH, 9, 173-179

Ilbert, O., et al., 2010, ApJ, 709, 644

Ivan, K., et al., 2004, ApJ, 600, 681

Jaderson, S., & Schimoia, 2017, MNRAS, 472, 2170

Jian, H. Y., et al., 2020, ApJ, 894, 125

Johnston, E. J., et al., 2012, MNRAS, 422, 2590

Juna, A., et al., 2006, ApJ, 648, 128

Karim, A., et al., 2011, ApJ ,730, 61

Karttunen, H., et al., 2003, Springer, 507

Katkov, I. Y., et al., 2015, AJ, 150, 24

Kauffmann G. et al., 2003, MNRAS, 341, 54

Kaviraj, S., 2010, MNRAS, 406, 382

Kennicutt Jr, R., et al., 1998, ARA&A, 36, 189

Kewley, L., et al., 2006, MNRAS, 372,961

Kewley, L., et al., 2019, ARA&A, 57, 511

Kocevski, D. D., et al., 2012, ApJ, 744, 148

Kovacević-Dojcinović, J., et al., 2022, Astrophys. J., Suppl. Ser, 262, 49

Labbé, I., et al., 2010, ApJL, 716, L103

Lakićević, M., et al., 2018, MNRAS, 478, 3

Larson, R. B., Tinsley, B. M., & Caldwell, C. N., 1980, ApJ, 237, 692

Leauthaud, A., et al., 2007, ApJS, 172, 219

Lee, G., et al., 2015, ApJ, 800, 80

Lennox, C., & Songaila, L. L., 1978, Nature, 266, 1476

Leslie, S. K., et al., 2016, MNRAS, 455, 82

Leslie, S. K., et al., 2020, ApJ, 899, 58

Lian, J. et al., 2017, MNRAS, 472, 4679

Liu, Y., et al., 2020, MNRAS, 497, 3011

Lucia, D. G., et al., 2006, MNRAS, 366, 499

Lusso, E., et al., 2019, A&A, 642, 150

Lutz, P., et al., 2011, A&A, 532, A90, 12

Madau, P., & Dickinson, M., 2014, arXiv:1403.0007

Mahoro, A., et al., 2017, MNRAS, 471, 3226

Mahoro, A., et al., 2019, MNRAS, 485, 452

Mahoro, A., et al., 2022, MNRAS, 4449, 513

Marconi, A., & Hunt, L. K., 2003, ApJ, 589, L21

Márquez, I., et al., 2017, Front. Astron. Space Sci., 4, 34

Martin, D. C., et al., 2017, ApJS, 173, 342

Mastropietro, M., et al., 2021, MNRAS, 504, 3387

Mata-Chávez, M. D., et al., 2019, ApJ, 876, 6

Mateos, S., et al., 2017, ApJL, 841, L18

Megan C., Urry, & Paolo P., 1995, PASP, 107, 803

Molino, A., et al., 2014, MNRAS, 441, 2891

Mullaney, J. R., et al., 2012, ApJ, 753, L30

Muñoz, L., et al., 2020, A&A, 635, A50

Nandra, K., et al., 2007, ApJ, 660, L11

Netzer, H., et al., 2015, ARAA, 53, 365

Netzer, H., et al., 2016, MNRAS, 462, 2878

Nogueira-Cavalcante, J. P., et al., 2018, MNRAS, 1346, 473

Nyiransengiyumva, B., et al., 2019, Proc Int Astron Union, 15, 152

Padovani, P., et al., 2017, A&A, 25, 60

Pan, Z., Kong X., Fan L., 2013, ApJ, 776, 14

Peng, Y., et al., 2010, ApJ, 721, 193

Phillipps, S., et al., 2019, MNRAS, 485, 5559

Poci, A., et al., 2021, A&A, 647, 145

Poggianti, M., et al., 2008, ApJ, 684, 888

Poglitsch, A., et al., 2010, A&A, 518, L2

Porter-Temple, R., et al., 2022, MNRAS, 515, 3875

Pović, M., et al., 2009a, ApJ, 702, 51

Pović, M., et al., 2009b, ApJ, 706, 810

Pović, M., et al., 2012, A&A, 541, A118

Pović, M., et al., 2013, MNRAS, 435, 3444

Pović, M., et al., 2016, MNRAS, 462, 2878

Premadi, P., et al., 2021, arXiv:2106.14581

Ptak, A., et al., 2007, ApJ, 667, 826

Rakshit, S., & Stalin, C. S., 2017, ApJ, 842, 96

Ramos Almeida, C., & Ricci, C., 2017, Nature Astronomy, 1, 679

Risaliti, G., & Elvis, M., et al., 2004, ApJ, 615, L25

Risaliti, G., & Lusso, E., 2019, NatAs, 3, 272

Rogers, B., et al., 2009, MNRAS, 399, 2172

Ross, N., et al., 2018, MNRAS, 480, 4468

Ruiz, A., et al. 2018, A&A, 618, 52

Saha, K., & Cortesi, A., 2018, ApJ, 862, 12

Salim, S., et al., 2007, ApJS, 173, 267

Salim, S., 2014, Serb. Astron. J., 189, 1

Salvestrini, F., et al., 2022, A&A, 663, A28

Schawinski, K., et al., 2010, ApJ, 711, 284

Schawinski, K., et al., 2014, MNRAS, 440, 889

Schneider, P., 2006, Springer, 44, 473

Schinner et al., 2010, ApJs, 11, 34

Scoville, N., et al., 2007, ApJS, 172, 38

Shankar, F., et al., 2019, Nature Astronomy, 4, 282

Shao, Z., et al., 2003, MNRAS, 338, 72

Shimizu, T., et al., 2015, MNRAS, 452, 1841

Shioya, Y., et al., 2002, ApJ, 565, 223

Sikora, M., et al., 2020, MNRAS, 499,3

Slijepcevic, I. V., et al., 2022, MNRAS, 514, 2599

Smethurst, R. J., et al., 2015, MNRAS, 450, 435

Smolčić, V., et al., 2017, A&A, 602, A2

Spengler, C., et al., 2017, ApJ, 849, 55

Tarrío, P., & Zarattini, S., 2020, A&A, 642, 102

Tasca, L. A. M., et al., 2009, A&A, 503, 379

Tommasin, S., et al., 2012, ApJ, 753, 155

Trayford, J., et al., 2016, MNRAS, 460, 3925

Trump, J., et al., 2013, ApJ, 763, 133

Urry Megan, C., & Padovan, P., 1995, PASP, 107, 803

Vardoulaki, E., et al., 2021, A&A, 648, 33

Veilleux, s., et al., 2005, ARAA, 43, 769

Wenderoth, E., et al., 2022, MNRAS, 515, 1052

Whitaker, K. E., et al., 2012, ApJL, 754, L29

Wilkins, S., & Stephen M., et al., 2022, MNRAS, tmp, 2400

Woods, T., et al., 2019, Astronomical Society of Australia, 36

Worthey, G., et al., 1994, ApJS, 95, 107

Xu, H., et al., 2018, MNRAS, 481, 5470

XueGuang, Z., 2022, ApJS, 261, 23

Zhang, Y., et al., 2021, MNRAS, 501, 1013

Zhu, P., et al., 2021, ApJ, 907, 6